1993ApJ...402..441L

THE ASTROPHYSICAL JOURNAL, 402:441–468, 1993 January 10
© 1993. The American Astronomical Society. All rights reserved. Printed in U.S.A.

SPECTROSCOPIC CONSTRAINTS ON THE PROPERTIES OF DUST IN ACTIVE GALACTIC NUCLEI

ARI LAOR
Institute for Advanced Study, Princeton, NJ 08540
AND
BRUCE T. DRAINE
Princeton University Observatory, Peyton Hall, Princeton, NJ 08544
Received 1992 April 3; accepted 1992 July 14

ABSTRACT

The lack of a significant silicate or silicon carbide emission feature in bright active galactic nuclei (AGNs) is used to constrain models in which the IR continuum is emitted by dust. We consider two models for the dust, a graphite + silicate grain mixture and a graphite + silicon carbide mixture. The optical properties of the grains are calculated using Mie theory, the Rayleigh-Gans approximation and geometric optics, for grains in the 0.005–10 μm size range, over the 1000 μm–1 Å wavelength range. We use these grain models to calculate the emission of optically thin and of optically thick dust, with various grain compositions, incorporating both absorption and scattering in the detailed radiative transfer. We find that $\sim 1:1$ mixtures of graphite + silicate grains of $a \lesssim 3$ μm in any configuration which is optically thin at 10 μm produce a very strong emission feature and are clearly ruled out. Optically thin dust must either be depleted of silicates by at least a factor of 5, or be composed mostly of grains as large as 10 μm. Dust with a large optical depth at 10 μm produces a significantly weaker emission feature, but its amplitude is still larger than the observational limits in most objects. This feature is washed out if the dust composition or grain size distribution are somewhat modified, or possibly if another heat source (e.g., stars) exists at a large optical depth inside the clouds. Similar results are obtained for a graphite + silicon carbide mixture. The different solutions to the absence of a silicate or silicon carbide emission feature can be further constrained using high S/N IR spectroscopy at 10 μm, X-ray spectroscopy, near-IR variability, and by looking for high ionization lines, or molecular lines from the associated gas.

The constraints on the dust configuration and composition imply the following: (1) the observed broad emission lines and continuum are unlikely to be noticeably reddened in most objects. (2) Dust cannot exist in the broad-line region clouds if their distance from the continuum source is smaller than $0.2L_{46}^{1/2}$ pc as recently indicated in a few objects. (3) Dust can exist in the narrow-line region clouds, and will have a strong effect on the narrow line flux if the ionization parameter $U \gtrsim 0.01$. (4) If the IR emission originates in clouds which are optically thick at 10 μm, then $U \gtrsim 0.1$ at the cloud surface.

We finally note that physical and dynamical arguments lead to similar constraints: small grains in an optically thin dust configuration are likely to be destroyed on a short time scale, while very large grains and grains in an optically thick cloud, both of which do not produce a pronounced emission feature, or reddening, are likely to survive longer.

Subject headings: dust, extinction — galaxies: active — galaxies: nuclei — infrared: interstellar: lines — radiative transfer

1. INTRODUCTION

About a third of the bolometric luminosity of quasars and bright Seyfert 1 galaxies, is emitted in the 1–100 μm range (Sanders et al. 1989). The emission mechanism is not yet established, but an attractive possibility is thermal reprocessing of the optical to far UV emission from the central continuum source by nearby dust, as originally proposed for Seyfert galaxies by Rees et al. (1969). This hypothesis is supported by a number of indirect lines of evidence: (1) the spectral turnover at $\lambda < 3$ μm (e.g., Neugebauer et al. 1979; Rieke & Lebofsky 1981; Rudy 1984; McAlary & Rieke 1988), and at $\lambda > 100$ μm (Barvainis 1987; Sanders et al. 1989). (2) Low-amplitude variability in the near-IR (Cutri et al. 1985; Neugebauer et al. 1989), and in the far-IR (Edelson & Malkan 1987), compared with the variability at $\lambda < 1$ μm. (3) Lack of significant polarization (Sitko & Zhu 1991). (4) Apparent reddening of the continuum and emission lines in some objects (see review by MacAlpine 1985). There are also a few objects in which the near-IR flux seemed to respond to variation in the visible-UV flux with a delay of a few months to about 1 year (Clavel, Wamsteker, & Glass 1989; Barvainis 1992; Baribaud et al. 1992; Glass 1992). Recent calculations have shown that the observed IR continuum can be fitted with optically thin dust in a spherical distribution (Barvainis 1987), and also with dust in a highly warped disk (Phinney 1989), or possibly optically thick dust in a torus (Pier & Krolik 1992).

IR spectroscopy of most bright AGNs does not, however, reveal features which can be associated with dust, although such features are observed in starburst galaxies and a few, mainly low-luminosity, AGNs (e.g., Roche et al. 1991). The absence of features associated with polycyclic aromatic hydrocarbons (PAHs) can be attributed to the presence of significant X-ray emission from AGNs, which effectively destroys carriers of these features up to a large distance, as recently shown by Voit (1991b). Features associated with icy mantles of a low binding energy are not expected due to the relatively high dust temperatures. The 9.7 μm silicate

© American Astronomical Society • Provided by the NASA Astrophysics Data System

1993ApJ...402..441L

feature is clearly seen in absorption in many starburst galaxies and a few AGNs. In most AGNs however the silicate feature is undetectable down to a level of 20%–50%. Since silicate grains are refractory and present in many galaxies, this fact is somewhat surprising.

The objective of this paper is to obtain constraints on the composition, size, and optical depth of dust in the central parts of AGNs, given the apparent absence of the 9.7 μm silicate feature. In § 2 we present the grain model, obtain dielectric functions for SiC, and extend the dielectric functions of graphite, silicate, and silicon carbide (SiC) to X-rays. We compute the optical properties of very large grains using Rayleigh-Gans theory and geometric optics, and calculate the extinction properties of dust with various grain size distributions. The method used to solve for the thermal emission of optically thin and optically thick dust is discussed in § 3, where we describe the solution of the radiative transfer in an optically thick slab with a range of grain sizes including both scattering and absorption. In § 4 we present the results for the emission of optically thin and optically thick dust. We show that optically thin "Galactic" graphite + silicate dust is ruled out, and obtain constraints on the possible dust composition and grain size distribution. The associated gas phase emission is discussed in § 5, and used to constrain the location and density of the dusty gas. Dynamical constraints based on radiation pressure effects are discussed in § 6, and in § 7 we briefly discuss processes which can modify the grain composition and size distribution. Section 8 discusses the implications of the various constraints made above on the possible dust reddening, other observational evidence for dust, and presents predictions for other observable effects. Our results are summarized in § 9.

The paper follows the cases of optically thin and optically thick dust in parallel. Readers who wish to follow each case separately should follow the optically thin case through §§ 3.1, 3.2, 4.1, 5.1, and 6.1, and the optically thick case via §§ 3.1, 3.3, 4.2, 5.2, and 6.2.

2. GRAIN MODEL

While the composition of interstellar dust in diffuse regions of the Galaxy is still controversial (see, e.g., Mathis 1988), the strong 9.7 and 18 μm absorption/emission features require that roughly 50% of the dust mass be contributed by some form of silicate mineral, probably amorphous. The composition of the remaining dust is less certain, but most researchers agree that some form of carbonaceous substance is required; graphite has received considerable attention as a candidate material.

On the basis of the strength of the interstellar 9.7 μm absorption feature amorphous silicate material is believed to account for $\sim 50\%$ of the interstellar grain mass (Draine & Lee 1984, hereafter DL); the 9.7 μm feature is observed in emission in H II regions, planetary nebulae, mass loss from M giant stars, and in protostars.

Graphite has been considered as an interstellar grain material because it is refractory and in order to explain the observed interstellar 2175 Å extinction feature (Draine 1989; Aannestad 1992).

Silicon carbide is made from relatively abundant elements, is highly refractory, has been identified in the outflows from some carbon stars (e.g., Treffers & Cohen 1974), and interstellar SiC grains have been found intact in "primitive" meteorites (e.g., Bernatowicz et al. 1987). Although not more than $\sim 5\%$ of the silicon in the local diffuse interstellar medium can be in SiC grains (Whittet, Duley, & Martin 1990), SiC presents an interesting alternative to silicate grains near AGNs.

We shall thus consider three possible materials for dust in AGNs: amorphous silicate with a composition like that of olivine; crystalline graphite; and SiC. The grains will be taken to be spherical. Absorption and scattering cross sections are required from infrared to X-ray wavelengths. Here we describe how these are calculated.

2.1. *Dielectric Functions*

The dielectric function $\epsilon = \epsilon_1 + i\epsilon_2$ is obtained by first adopting $\epsilon_2(\omega)$ at all wavelengths, and then computing ϵ_1 from ϵ_2 using the Kramers-Kronig relation

$$\epsilon_1(\omega) = 1 + \frac{2}{\pi} P \int_0^\infty \frac{x\epsilon_2(x)}{x^2 - \omega^2}\, dx\,, \tag{1}$$

where $\omega = 2\pi c/\lambda$ (Landau, Lifshitz, & Pitaevskii 1984).

At X-ray wavelengths, we estimate the dielectric functions by taking

$$\epsilon_2 \approx \frac{\lambda}{2\pi} \sum_{jnl} n_j \sigma_{jnl}\left(\frac{hc}{\lambda}\right)\,; \tag{2}$$

here the sum runs over the subshells nl of each element j present, n_j is the number density of atoms of element j in the solid, and $\sigma_j(E)$ is the gas-phase photoelectric absorption cross section for an atom of element j. Equation (2), also used by Martin & Rouleau (1991), should be quite accurate for $h\nu \gtrsim 100$ eV, and should provide a reasonable estimate for ϵ_2 for $h\nu \gtrsim 25$ eV. The photoelectric absorption cross sections σ_j are estimated using the empirical fitting formula of Woods & Draine (1993):

$$\sigma_{jnl}(E) = A\left(\frac{E}{E^T}\right)^{-a} \exp\left\{b\left[1 - \frac{E^T}{E}\right] + \frac{c}{2}\left[1 - \left(\frac{E^T}{E}\right)^2\right]\right\}. \tag{3}$$

The parameters E^T, A, a, b, and c are taken from Woods & Draine (1993), except that for all subshells except the valence shell we have adjusted the multiplicative coefficient A so that the total oscillator strength $(m_e c/\pi e^2 h)\int \sigma(E)dE$ associated with each subshell is equal to the number of electrons in that subshell. The parameters used here are given in Table 1.

For "astronomical silicate" and $h\nu < 17$ eV we take ϵ_2 from DL; for $h\nu > 20$ eV we use equations (2) and (3), for an assumed density $\rho = 3.3$ g cm^{-3} and composition $MgFeSiO_4$. From 17–20 eV we make a smooth join to the experimental data of Huffman (1975). The adopted ϵ_2 is shown in Figure 1, together with the resulting ϵ_1.

© American Astronomical Society • Provided by the NASA Astrophysics Data System

1993ApJ...402..441L

TABLE 1

SUBSHELL PHOTOELECTRIC CROSS SECTIONS

$X(nl)$	E^T (eV)	A (10^{-18} cm^2)	a	b	c
C(2s2p)	11.3	12.40	2.6120	4.3860	−2.6960
C(1s)	280.0	1.08	3.0860	0.6560	0.6990
O(2s2p)	13.6	9.59	2.809	6.396	−3.215
O(1s)	533.0	0.572	2.870	−0.710	2.073
Mg(3s)	7.6	0.151	3.7240	17.850	−16.43
Mg(2p)	54.0	1.07	3.2700	−1.101	11.890
Mg(2s)	92.2	0.969	2.5210	2.9290	−0.639
Mg(1s)	1320.0	0.275	3.2020	1.3040	−0.6130
Si(3s3p)	8.1	34.4	2.6270	15.440	−24.7100
Si(2p)	116.0	5.25	2.9650	1.0030	1.2850
Si(2s)	168.0	1.17	2.5030	0.9040	0.3840
Si(1s)	1870.0	0.192	3.0420	0.6490	−0.0160
Fe(4s3d)	7.9	3.4480	3.0380	20.820	−22.6400
Fe(3p)	65.2	2.47	4.2500	18.430	−18.1500
Fe(3s)	96.5	0.898	3.0280	6.6710	−4.5370
Fe(2p)	741.0	1.48	4.1090	2.1690	0.0000
Fe(2s)	836.0	0.260	4.2330	3.7610	0.0000

For graphite ($\rho = 2.26$ g cm^{-3}) with $E \parallel c$ and $h\nu < 21$ eV we take ϵ_2 from DL; for $h\nu > 23$ eV we use equations (2) and (3); and for 21–23 eV we make a smooth join to the experimental values of Tosatti & Bassani (1970). For $E \perp c$ and $h\nu < 31$ eV we take ϵ_2 from DL; for $h\nu > 34$ eV we use equations (2) and (3); for 31–34 eV we make a smooth join to the experimental values of Tosatti & Bassani (1970).

For SiC ($\rho = 3.22$ g cm^{-3}) we use equations (2) and (3) to estimate ϵ_2 for $h\nu > 12$ eV; for 4–10 eV we use the experimental ϵ_2 from Philipp & Taft (1969); and from 10–12 eV we make a smooth join between the two. SiC has a strong lattice resonance near 12 μm. Pegourie (1988) constructed a synthetic dielectric function to reproduce various laboratory measurements on SiC, including those of Borghesi et al. (1985, 1986). Unfortunately, as noted by Pegourie, it does not appear to be possible to reconcile all of the different laboratory experiments; the dielectric function thus obtained by Pegourie is very different from that derived by Bohren & Huffman (1983) from reflectivity measurements on α-SiC. In view of the large uncertainties we take ϵ_2 in the infrared to be given by a sum of

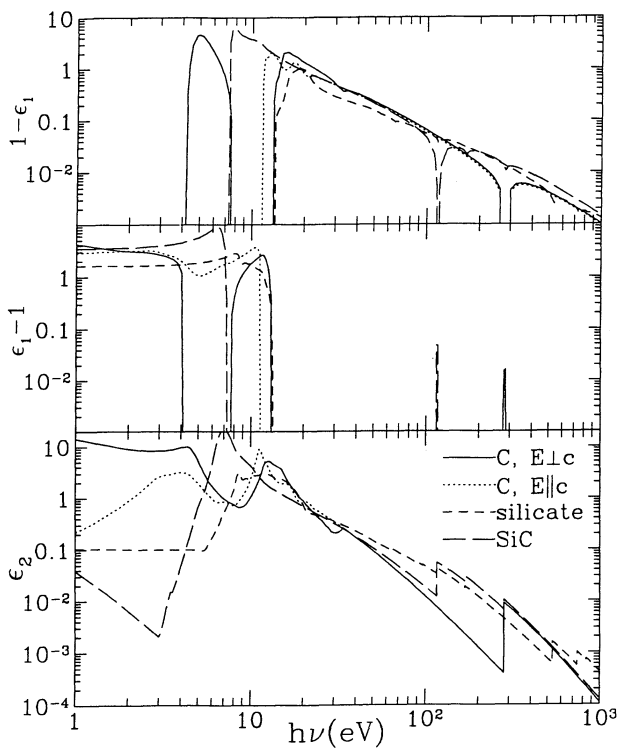

FIG. 1.—Real and imaginary components of the complex dielectric function $\epsilon_1 + i\epsilon_2$ for graphite, silicate, and SiC grains. Strong absorption edges are apparent at 116 eV (Si $2p^6$), 280 eV (C $1s^2$), 533 eV (O $1s^2$), and 741 eV (Fe $2p^6$).

© American Astronomical Society • Provided by the NASA Astrophysics Data System

1993ApJ...402..441L

the contributions from N damped oscillators:

$$\epsilon_2 = \sum_{j=1}^{N} \mathrm{Im}\left[\frac{S_j}{1-(\lambda_j/\lambda)^2 - i\Gamma_j(\lambda_j/\lambda)}\right]. \tag{4}$$

Bohren & Huffman (1983) argue that the infrared response of the lattice is satisfactorily reproduced by a single oscillator with $\lambda_1^{-1} = 793\ \mathrm{cm}^{-1}$, $S = 3.3$, and $\Gamma_1 = 0.0060$. This resonance is very much narrower than the dielectric function adopted by Pegourie, which has both a broader resonance peak plus additional absorption extending from the near-IR longwards. For purposes of illustration here we adopt a dielectric function with a resonance peak with the same central frequency $\lambda_1^{-1} = 793\ \mathrm{cm}^{-1}$ and strength $S_1 = 3.3$ recommended by Bohren and Huffman, but considerably broadened, with $\Gamma_1 = 0.1$; in addition we include "continuum" absorption represented by a highly damped oscillator with $S_2 = 1$, $\Gamma_2 = 3$, and with a "resonant" frequency $\lambda_2^{-1} = 2158\ \mathrm{cm}^{-1}$ chosen so that its contribution to ϵ_2 peaks at $793\ \mathrm{cm}^{-1}$. The resulting dielectric function is shown in Figure 1.

2.2. *Grain Optics*

For purposes of calculating absorption and scattering efficiencies Q_{abs} and Q_{sca} for spherical particles we use the standard Mie series expansion, provided $|m|x < 1000$, where $m = \epsilon^{1/2}$ is the complex refractive index, and $x = 2\pi a/\lambda$ is the usual "scattering parameter". In the case of graphite, a highly anisotropic material, we make the usual "$\frac{1}{3}$–$\frac{2}{3}$" approximation: we assume that $\frac{2}{3}$ of the randomly oriented graphite grains may be represented by spheres with an isotropic dielectric function $\epsilon = \epsilon(E \perp c)$, and the other $\frac{1}{3}$ are represented by spheres with $\epsilon = \epsilon(E \parallel c)$. While difficult to justify (except in the limit $x \to 0$) this approximation has been found to be surprisingly accurate (Draine 1988). Here we are also interested in combinations of large grains and short wavelengths (e.g., $a = 10\ \mu\mathrm{m}$, $\lambda = 100$ Å, $x = 6300$), and for large values of $|m|x$ the Mie series expansion becomes difficult to evaluate accurately. We must therefore resort to approximations.

2.2.1. *The Rayleigh-Gans Regime*

For $|m|x > 1000$ and $|m-1|x < 0.001$ we use Rayleigh-Gans theory (Bohren & Huffman 1983). For Q_{abs} we take

$$Q_{\mathrm{abs}} \approx \tfrac{8}{3}\,\mathrm{Im}\,(m)x\ . \tag{5}$$

In the Rayleigh-Gans limit the exact result for Q_{sca} is

$$Q_{\mathrm{sca}} = |m-1|^2\left\{\frac{5}{2} + 2x^2 - \frac{\sin 4x}{4x} - \frac{7}{16x^2}(1-\cos 4x) + \left(\frac{1}{2x^2} - 2\right)\left(\gamma + \ln 4x + \int_{4x}^{\infty} u^{-1}\cos u\,du\right)\right\}, \tag{6}$$

where $\gamma = 0.57721\ldots$ is Euler's constant (van de Hulst 1957). We approximate equation (6) by

$$Q_{\mathrm{sca}} \approx \frac{32|m-1|^2x^4}{27+16x^2}, \tag{7}$$

which has the correct limiting behavior for $x \ll 1$ and $x \gg 1$, and is accurate to within $+4.6\%$, -8.5% for $0 < x < \infty$. For the scattering asymmetry factor we take

$$g \equiv \langle\cos\theta\rangle \approx \frac{0.3x^2}{1+0.3x^2}, \tag{8}$$

which reproduces the numerical results of Ryde & Cooper (1931; quoted by van de Hulst 1957) to within $+0.07$, -0.08 for $0 < x < \infty$.

2.2.2. *The Geometric Optics Regime*

If $|m|x > 1000$, and $|m-1|x > 0.001$ we use an approximate treatment based on geometric optics. Consider a ray incident on the surface of the sphere, with impact parameter $b < a$. We consider separately the two polarization states with E field parallel and perpendicular to the plane defined by the incident ray and the surface normal. Stratton (1941) has discussed the reflection of electromagnetic plane waves at a planar interface. Define the functions

$$\tilde{p}^2(\theta) \equiv \tfrac{1}{2}[\sin^2\theta - \mathrm{Re}\,(\tilde{\epsilon}) + \{[2\,\mathrm{Im}\,(\tilde{\epsilon})]^2 + [\mathrm{Re}\,(\tilde{\epsilon}) - \sin^2\theta]^2\}^{1/2}], \tag{9}$$

$$\tilde{q}^2(\theta) \equiv \tfrac{1}{2}[\mathrm{Re}\,(\tilde{\epsilon}) - \sin^2\theta + \{[2\,\mathrm{Im}\,(\tilde{\epsilon})]^2 + [\mathrm{Re}\,(\tilde{\epsilon}) - \sin^2\theta]^2\}^{1/2}], \tag{10}$$

where θ is the angle of the incident ray relative to the normal, and $\tilde{\epsilon}$ is the ratio of the dielectric function of the second medium to that of the first. The reflection coefficients for E field perpendicular and parallel to the reflection plane are then

$$R_{\perp} = \frac{(\tilde{q}-\cos\theta)^2 + \tilde{p}^2}{(\tilde{q}+\cos\theta)^2 + \tilde{p}^2}, \tag{11}$$

$$R_{0,\parallel} = R_{0,\perp}\left[\frac{(\tilde{q}-\sin\theta\tan\theta)^2 + \tilde{p}^2}{(\tilde{q}+\sin\theta\tan\theta)^2 + \tilde{p}^2}\right]. \tag{12}$$

Consider the ray (in *vacuo*) incident with impact parameter b on a grain of radius a and dielectric function ϵ. For the initial reflection/transmission we have $\tilde{\epsilon} = \epsilon$, and $\theta = \theta_0$, where

$$\theta_0 \equiv \sin^{-1}(b/a), \tag{13}$$

© American Astronomical Society • Provided by the NASA Astrophysics Data System

1993ApJ...402..441L

and we use equations (9)–(12) to evaluate the two reflection coefficients $R_{0,\parallel}$, $R_{0,\perp}$. The refracted wave enters the sphere at an angle ψ to the normal, where ψ is determined by the generalized Snell's law:

$$\sin\psi = \frac{\sin\theta_0}{[\tilde{q}^2(\theta_0) + \sin^2\theta_0]^{1/2}} . \tag{14}$$

After traveling a distance $2a\cos\psi$ in the target, the ray reaches the target surface after attenuation by a factor A. At this surface the two polarization states have probabilities $R_{1,\parallel}$, $R_{1,\perp}$ of internal reflection, these reflection coefficients being given by equations (11)–(12) evaluated with $\tilde{\epsilon} = \epsilon^{-1}$ and $\theta = \psi$. Subsequent internal reflections occur at the same angle and with the same reflection coefficients; summing over the infinite series of internal reflections we obtain

$$Q_{\rm abs} = \int_0^{\pi/2} \sin\theta_0 \cos\theta_0 \, d\theta_0 (1 - A)\left[\frac{1 - R_{0,\perp}}{1 - AR_{1,\perp}} + \frac{1 - R_{0,\parallel}}{1 - AR_{1,\parallel}}\right], \tag{15}$$

where

$$A(\theta_0) = \exp\left[-8\pi a \,\mathrm{Im}\,(m)\cos\psi/\lambda\right] . \tag{16}$$

Strictly speaking, "geometric optics" is only applicable when $x \gg 1$ *and* $|m - 1|x \gg 1$, in which case we have the familiar limiting result $Q_{\rm ext} \approx 2$. In the present application we resort to "geometric optics" when $x > 10^3$; since $|m - 1|$ may be small we are not necessarily in the true geometric optics limit. In order to ensure reasonable (if not accurate) behavior we take

$$Q_{\rm ext} \approx \frac{Q_{\rm RG}}{(1 + 0.25Q_{\rm RG}^2)^{1/2}} , \tag{17}$$

where

$$Q_{\rm RG} = \frac{32|m - 1|^2x^4}{27 + 16x^2} + \frac{8}{3}\,\mathrm{Im}\,(m)x \tag{18}$$

is the "Rayleigh-Gans" estimate for $Q_{\rm ext}$; equation (17) is designed so that $Q_{\rm ext} \approx 2$ for $|m - 1|x \gtrsim 1$. With $Q_{\rm ext}$ from equation (17) and $Q_{\rm abs}$ from equation (15) we calculate the scattering efficiency

$$Q_{\rm sca} = Q_{\rm ext} - Q_{\rm abs} . \tag{19}$$

We estimate the scattering asymmetry factor by summing over external reflection and transmission with zero or one internal reflections:

$$g = Q_{\rm sca}^{-1}\int_0^{\pi/2} \sin\theta_0\cos\theta_0\, d\theta_0\left[(R_{0,\perp} + R_{0,\parallel})\cos(2\theta_0) + \sum_{n=0}^{1} h_n(\theta_0)\right], \tag{20}$$

where

$$h_n(\theta_0) = A^{n+1}\cos\left[2(\theta_0 - \psi) + n(\pi - 2\psi)\right]\sum_{j=\parallel,\perp}(1 - R_{0,j})R_{1,j}^n(1 - R_{1,j}) . \tag{21}$$

The sum is over the number n of internal reflections. We neglect $n \geq 2$ internal reflections because: (1) the probability of multiple internal reflections is likely to be small, since the probability of n internal reflections is $\propto(1 - R_0)(1 - R_1)R_1^n A^{n+1}$; (2) the scattering associated with multiple internal reflections is likely to be moderately isotropic. In our numerical calculations we evaluate the integrals in equations (15) and (20) using 16 point Gaussian quadrature.

Absorption and scattering properties calculated using the above techniques are shown in Figures 2–4 for graphite, silicate, and SiC grains of various sizes.

Figure 5 shows $Q_{\rm abs}/a$ for silicate and SiC grains in the 3–30 μm region. For $a \leq 0.1$ μm $Q_{\rm abs}/a$ (proportional to the absorption cross section per unit mass) is independent of a, and the 9.7 μm silicate feature and 10.6 μm SiC feature are prominent. For $a \gtrsim 3$ μm, however, the individual grains become "optically thick" to resonance photons, and $Q_{\rm abs}/a$ is reduced relative to the small particle limit. For $a > 3$ μm neither the 9.7 μm silicate feature, nor the 10.6 μm SiC feature are recognizeable.

2.3. *Dust Models*

The Galactic extinction law in the diffuse interstellar medium (ISM) is well reproduced by the Mathis, Rumpl, & Nordsieck (1977, hereafter MRN) graphite + silicate grain mixture over the 1000 Å–10 μm range (DL). In this model the grains have a power-law size distribution of the form

$$dn_i(a) = A_i n_{\rm H} a^\beta \, da \qquad (a_{\rm min} \leq a \leq a_{\rm max}) , \tag{22}$$

where $dn_i(a)$ is the number density of grains of composition i [either graphite (gra), silicate (sil) or silicon carbide (SiC)], with radii in the interval $[a, a + da]$, and $n_{\rm H}$ is the number density of H nuclei.

The grain mass per H mass f_d (for $\beta \neq -4$) is

$$f_d = \frac{4\pi}{3m_{\rm H}}\frac{a_{\rm max}^{\beta+4}}{(\beta + 4)}\left[1 - \left(\frac{a_{\rm min}}{a_{\rm max}}\right)^{\beta+4}\right]\sum_i A_i\rho_i , \tag{23}$$

© American Astronomical Society • Provided by the NASA Astrophysics Data System

1993ApJ...402..441L

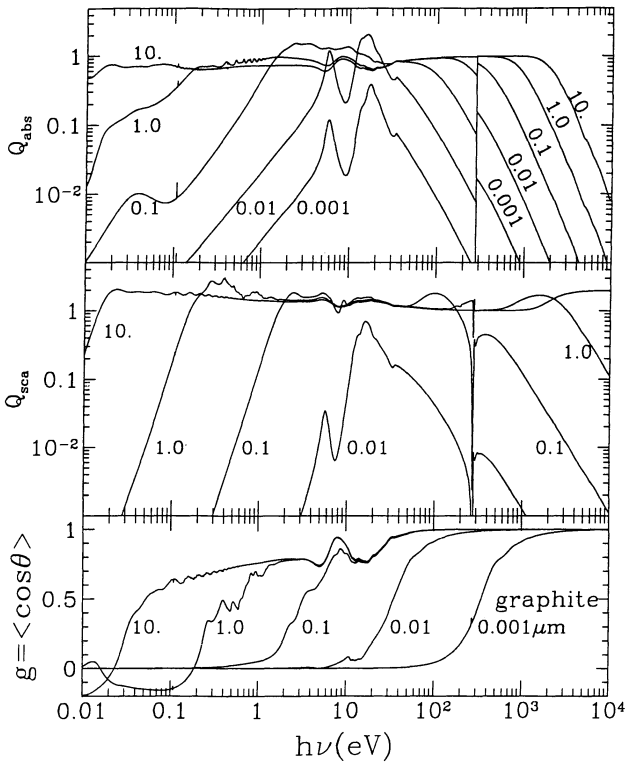

FIG. 2

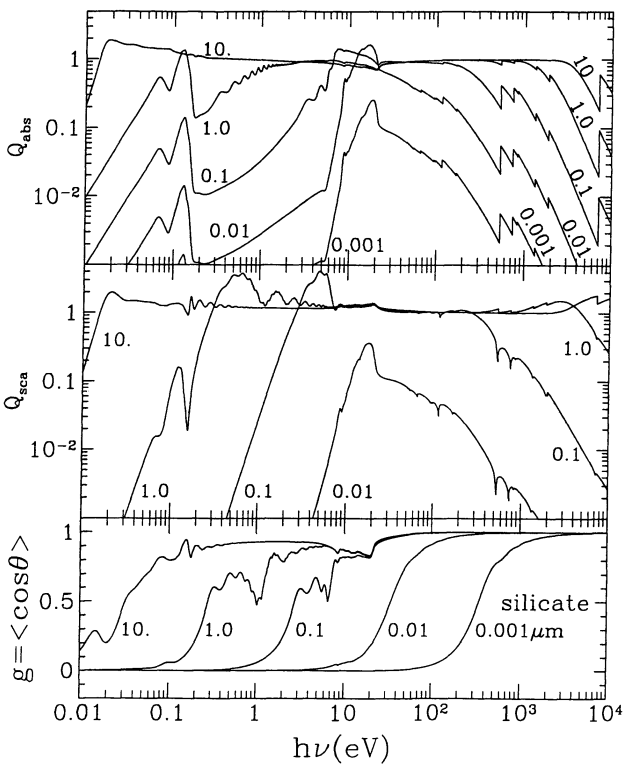

FIG. 3

FIG. 2.—Optical properties of spherical graphite grains of various radii a. $Q_{abs} = C_{abs}/\pi a^2$ and $Q_{sca} = C_{sca}/\pi a^2$ are the usual absorption and scattering efficiency factors, where C_{abs} and C_{sca} are the absorption and scattering cross sections, respectively. Curves are labeled by grain radius a (in μm). Lower panel shows the scattering asymmetry factor $g = \langle \cos\theta \rangle$, where θ is the scattering angle.

FIG. 3.—Same as Fig. 2, but for silicate grains

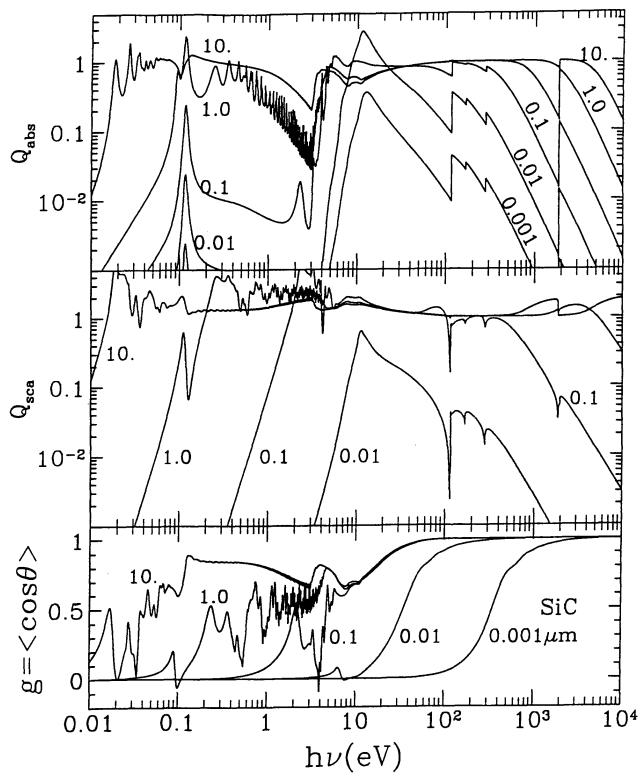

FIG. 4

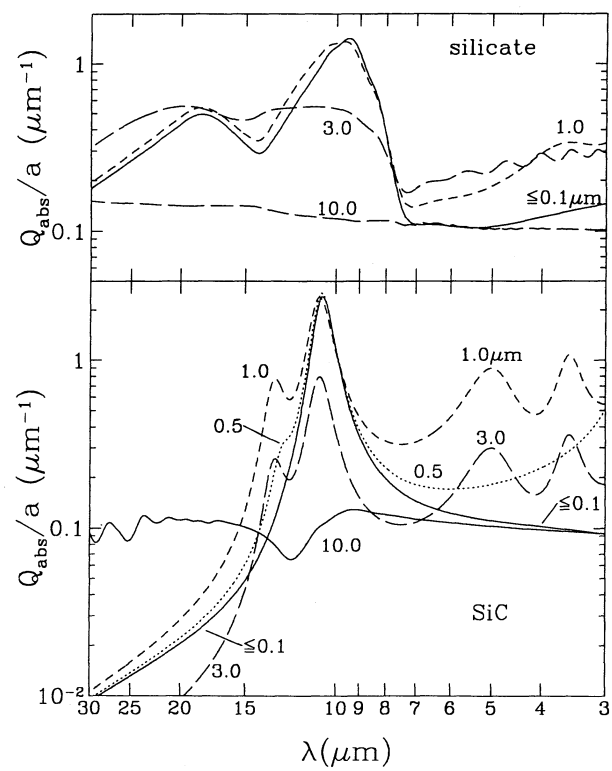

FIG. 5

FIG. 4.—Same as Fig. 2, but for SiC grains

FIG. 5.—Q_{abs}/a for silicate and SiC grains in neighborhood of strong IR absorption features, for grains of various radii. Curves are labeled by radius a (μm). It is seen that the 9.7 μm silicate and 10.6 μm SiC absorption features are prominent for silicate grains with $a \leq 1$ μm, but are strongly suppressed for $a \geq 10$ μm.

© American Astronomical Society • Provided by the NASA Astrophysics Data System

1993ApJ...402..441L

where ρ_i is the density of solid i. For graphite + silicate mixtures we take $f_d = 0.01$ and $A_{sil}/A_{gra} = 1.12$ (DL); the graphite + silicate mixture with $a_{min} = 0.005$ μm, $a_{max} = 0.25$ μm, and $\beta = -3.5$ will be referred to as "MRN dust". For graphite + SiC mixtures we take $f_d = 0.0058$ and $A_{SiC}/A_{gra} = 0.23$, corresponding to complete condensation of solar abundance Si and C into SiC and graphite.

The dust extinction coefficient is

$$\alpha_\nu^{ext} = \int_{a_{min}}^{a_{max}} \pi a^2 \left[\sum_i Q_{ext}^i(a, \nu) \frac{dn}{da} \right] da \, . \tag{24}$$

The absorption curve of graphite + silicate dust with the MRN size distribution is displayed in Figure 6*a*, together with absorption curves for other size distributions. Figure 6*b* displays the absorption curve of graphite + SiC dust with the same size distributions. The extension of a_{max} to 10 μm reduces the dust UV opacity by about an order of magnitude, as most of the mass is now locked up in

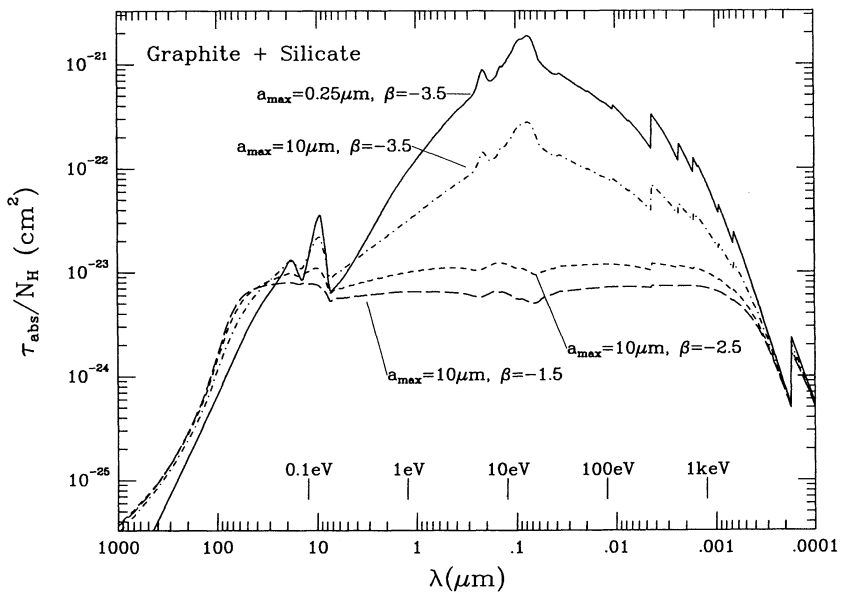

FIG. 6*a*

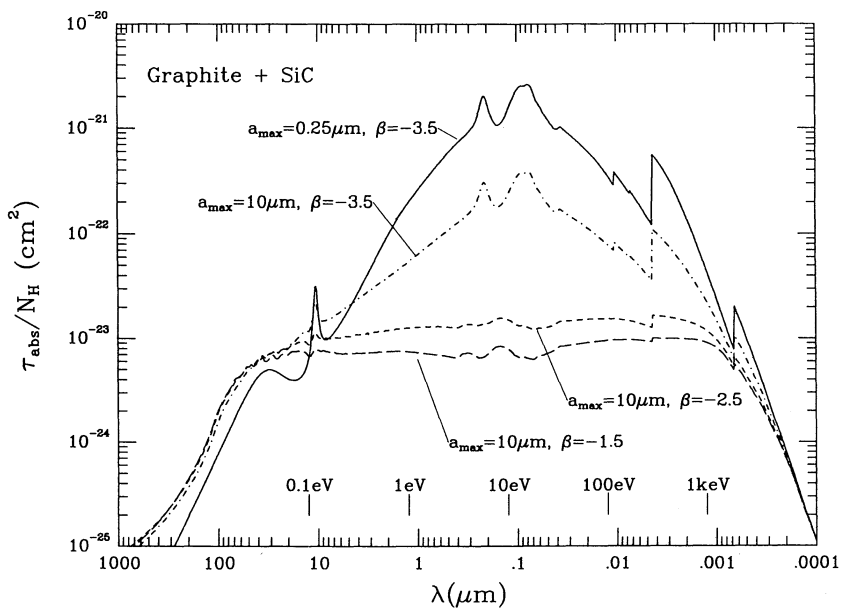

FIG. 6*b*

FIG. 6.—(*a*) Absorption cross section per H nucleus calculated for the MRN mixture of graphite and silicate spheres with a dust to H mass of 100. The size distribution extends from $a_{min} = 0.005$ μm to $a_{max} = 0.25$ μm in the upper curve, and to $a_{max} = 10$ μm in the lower three curves, the slopes of the power law size distributions are indicated in the figure. Note the reduction in the UV opacity when large grains are present, due to the decrease in the number of small grains. Dust with $\beta = -2.5$ and -1.5 is a nearly gray absorber over more than four wavelength decades. At a few keV all grains become transparent, the absorption is therefore proportional to the total grain mass, and all dust distributions converge. (*b*) Same as Fig. 6*a*, for a graphite + SiC grain mixture with $A_{SiC}/A_{gra} = 0.23$.

© American Astronomical Society • Provided by the NASA Astrophysics Data System

1993ApJ...402..441L

a few very large grains. Changing the size distribution power-law exponent to -2.5 and -1.5 reduces further the small to large grain abundance, and results in essentially gray absorption over the 10 μm–10 Å range. All absorption curves converge in the X-ray range since the absorption at these wavelengths is proportional to the total grain mass.

A number of recent observations indicate that the grain size distribution in the ISM extends well below 50 Å (e.g., Puget & Leger 1989). These grains are subject to large temperature fluctuations (Greenberg 1968; Duley 1973; Greenberg & Hong 1974; Purcell 1976; Draine & Anderson 1985; Guhathakurta & Draine 1989) resulting in continuum emission differing from that for grains in equilibrium. Voit (1991b) has recently shown that grains with $a \leq 10$ Å are efficiently destroyed by the X-ray flux of the AGN. Grains in the range 10 Å $\leq a \leq 50$ Å are not destroyed, but the excess nonequilibrium continuum emission of these grains at short wavelengths carries only a small fraction of the total grain emission. The equilibrium emission of hotter grains will dominate over this nonequilibrium emission, and we therefore neglect the effects of such temperature fluctuations. Note also that at small enough distances the size distribution will be modified as grains near the lower size cutoff sublime (see § 3.2), resulting in increasing $a_{\rm min}$ with decreasing r.

Below we assume all grains are at their steady-state temperature. We assume that all silicate and SiC grains sublime above 1400 K, and graphite grains above 1750 K. Apart from the graphite + silicate MRN mixture we also consider below a graphite + SiC mixture as a candidate for dust in AGNs. This composition can also reproduce an extinction law similar to that observed in the ISM, as demonstrated by MRN, though it does not constitute a significant component of the diffuse dust in the Galaxy. We note that while there are a number of alternative models for the grain composition in the diffuse ISM (Mathis 1990), the optical properties of the grains in these other models are not yet defined to the required level of accuracy, hence we do not discuss them in this paper.

2.4. *Gas Phase Absorption*

In all the calculations below we assume that dust is the only continuum absorption opacity source present. This is generally justified at $\lambda > 911.8$ Å when free-free and other gas phase absorption is negligible. Beyond the Lyman limit this assumption is justified if H and He are sufficiently highly ionized; while this is probably the case if the dust is optically thin, it does not necessarily hold if the dust resides in dense optically thick clouds. The constraints on the gas phase absorption are further discussed in § 5, where we show that the dust opacity must dominate beyond the Lyman limit too.

The opacity of a solar abundance cold gas to X-rays above 0.5 keV is mainly due to absorption by metals (Morrison & McCammon 1983) either in the gas phase or inside grains. A photon absorbed in the gas phase results in a fast photoelectron (and possibly Auger electrons) and atomic recombination and fluorescence lines, which are likely to be absorbed by the grains. The fast electrons will either degrade their energy by heating the gas, or by exciting various atomic and molecular levels (e.g., Voit 1991a), in which case UV, optical and IR lines produced by deexcitation will also be absorbed by the dust. X-ray photons absorbed inside grains will produce fast electrons which will deposit most of their energy inside the grain (Voit 1991b). A detailed treatment of the X-ray radiative transfer is beyond the scope of this paper, but the assumption adopted here that all the X-ray energy is eventually absorbed in the grains should provide a reasonable approximation.

We also note that the total flux in X-rays which are efficiently absorbed by dust is typically only a few percent of the central continuum source bolometric flux (see § 3.1).

3. METHOD OF SOLUTION

3.1. *The Incident Continuum*

The following sections present the methods used to calculate the emission of dust heated by an external continuum source. The assumed continuum energy distribution, shown in Figure 7, is based mainly on data available for optically selected quasars, and is very similar to the average continuum shape displayed by Sanders et al. (1989). The continuum shape in the 1000–30 Å range is uncertain, but the shape adopted here is consistent with constraints on the $\lambda < 911.8$ Å spectrum obtained from photoionization calculations applied for the broad-line region (e.g., Mathews & Ferland 1987). We take into account the continuum from $\lambda_{\rm max} =$ 1000 μm to $\lambda_{\rm min} = 1$ Å; negligible power is emitted longward of $\lambda_{\rm max}$. Very little data are available shortward of $\lambda_{\rm min}$, and in some objects a significant fraction of the total power might be emitted at hard X-rays and gamma rays (Hartman et al. 1992). The dust opacity at $\lambda < 1$ Å is, however, smaller by at least a factor of 10 than the opacity around 10 μm (cf. Fig. 6), so hard X-ray heating would therefore have only a small direct effect on the energy balance in the layer from which the silicate feature is emitted.

In the case of optically thin dust along our line of sight to the continuum source the observed continuum will be reddened. The intrinsic optical–UV slope should therefore be flatter than -0.5 (i.e., $d\ln L_\nu/d\ln\nu > -0.5$). We assume in this case that the optical–UV slope is -0.35 (see § 4.1.1), and arbitrarily extend it to $\lambda > 1.2$ μm; note however that the IR continuum shape is unimportant since the dust is highly transparent there. In the case of optically thick dust the shape of the energy distribution in the IR can have a significant effect on the amplitude of the silicate feature. For this case we use the continuum shown in Figure 7. This energy distribution shows a "break" in the power-law slope at $\lambda = 1.2$ μm; we use this wavelength to separate the component which presumably originates in the central part of the AGN, assumed here to be a point source, from the IR emission which we assume originates from other dust clouds, and is taken here to be incident from a solid angle of 2π. The specific intensity of the incident radiation is therefore

$$I_\nu^*(\mu,\,\phi) = \begin{cases} \delta(\mu-\mu_{\rm in})\delta(\phi-\phi_{\rm in})L_\nu/4\pi r^2 & \lambda \leq 1.2\ \mu{\rm m} \\ H(\mu)L_\nu/8\pi^2 r^2 & \lambda > 1.2\ \mu{\rm m} \end{cases}, \tag{25}$$

where $\theta_{\rm in} = \cos^{-1}\mu_{\rm in}$ is the angle of the continuum point source from the normal to the slab, $\phi_{\rm in}$ is an arbitrary azimuthal angle, and $H(\mu)$ is the Heaviside unit step function.

© American Astronomical Society • Provided by the NASA Astrophysics Data System

1993ApJ...402..441L

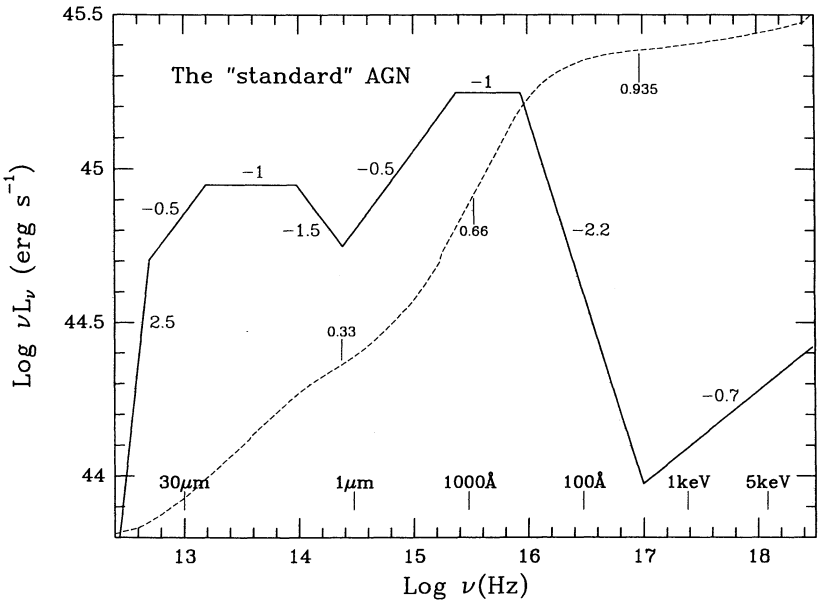

FIG. 7.—Spectral energy distribution of a "standard" AGN with $L_{bol} = 10^{46}$ ergs s^{-1}. This shape is based mainly on continuum data of the PG sample quasars. The continuum shape in the 1000–30 Å range is uncertain. The thin dotted line indicates the fraction of the bolometric flux integrated from low frequencies. The IR luminosity below the power law break at $\lambda = 1.2$ μm is 33% of the bolometric luminosity. A further 33% is emitted at 1.2 μm $< \lambda <$ 800 Å. Only 6.5% is emitted in the 0.4–12 keV range. X-rays at higher energy are absorbed at $\tau_{9.7\ \mu m} > 10$ (see text), and are not likely to have a significant effect on the emitted spectrum at 10 μm.

3.2. "*Optically Thin*" *Dust*

Below we follow the case of "optically thin" dust, where by "optically thin" we refer to dust which is optically thin to its own thermal emission.

The steady-state temperature, $T_i(a, r)$, of a grain of composition i, radius a, with an absorption efficiency $Q^i_{abs}(a, \nu)$, at a distance r from a continuum source, is determined by equating the grain heating by photon absorption to cooling by photon emission:

$$\int_0^\infty \frac{L_\nu}{4\pi r^2}\, e^{-\tau_\nu(r)} Q^i_{abs}(a, \nu) d\nu = \int_0^\infty 4\pi B_\nu[(T_i(a, r)] Q^i_{abs}(a, \nu) d\nu\ , \tag{26}$$

where $L_\nu\, d\nu$ is the luminosity of the central point source in $[\nu, \nu + d\nu]$, and

$$\tau_\nu(r) = \int_0^r \alpha_\nu^{abs}(r') dr' \tag{27}$$

is the optical depth from the central source to r, where the dust absorption coefficient, $\alpha_\nu^{abs}(r')$, is a function of radius, since the gas density, $n_H(r)$, varies with distance according to the following relation:

$$n_H(r) = n_H^0 \left(\frac{r}{r_0}\right)^\gamma \qquad (r_{in} \le r \le r_{out})\ . \tag{28}$$

Note that we use the absorption, rather than the extinction opacity, as scattering does not extinguish the flux to first order in τ in a spherically symmetric configuration.

Figure 8 presents $T_i(a, r)$ of a single silicate or graphite grain illuminated by the continuum shown in Figure 7 with a bolometric luminosity, $L_{bol} \equiv \int_0^\infty L_\nu\, d\nu = 10^{46} L_{46}$ ergs s^{-1}. The temperature of the smallest grains considered, 0.005 μm, is typically twice the temperature of the 0.25 μm grains, and about 3–5 times that of the local blackbody temperature, while the temperature of very large grains is usually close to that of a blackbody. Note the very large range of sublimation radii: small silicate grains evaporate rapidly at $r < 4L_{46}^{1/2}$ pc, while larger grains survive down to $0.2L_{46}^{1/2}$ pc. Note also the large difference in temperature of silicate and graphite grains, in particular around $100L_{46}^{1/2}$ pc. This results from the enhanced emissivity of silicates near 10 μm, versus a local minimum in the graphite emissivity in the same region (Figs. 2 and 3).

Figure 9 presents the continuum emission of silicate and graphite grains of various sizes at a distance of $5L_{46}^{1/2}$ pc. The large range in grain temperatures and emissivities results in significant variations in their continuum emission. This clearly demonstrates that models which incorporate a single grain size, and a single grain composition, will generally not provide a good approximation for the local grain emission.

The luminosity of a spherically symmetric distribution of grains extending from r_{in} to r_{out} is given by

$$L_\nu^{gr} = \int_{r_{in}}^{r_{out}} 4\pi r^2\, dr \int_{a_{min}}^{a_{max}} 4\pi^2 a^2 \left\{\sum_i B_\nu[T_i(a, r)] Q^i_{abs}(a, \nu) \frac{dn_i(a, r)}{da}\right\} da\ . \tag{29}$$

© American Astronomical Society • Provided by the NASA Astrophysics Data System

1993ApJ...402..441L

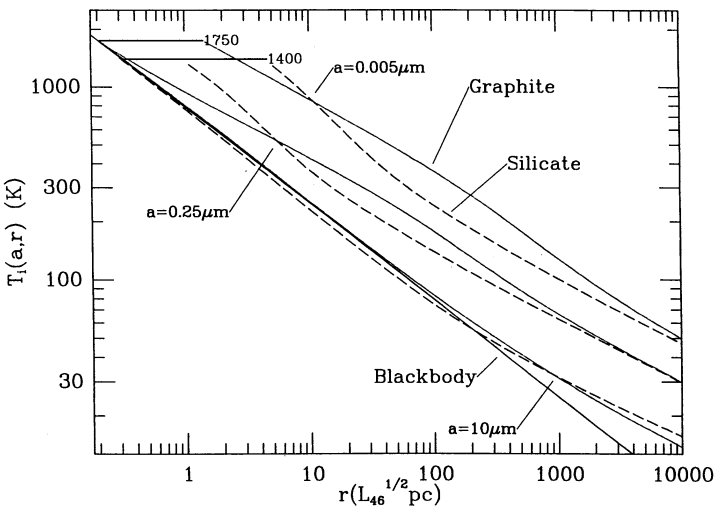

FIG. 8

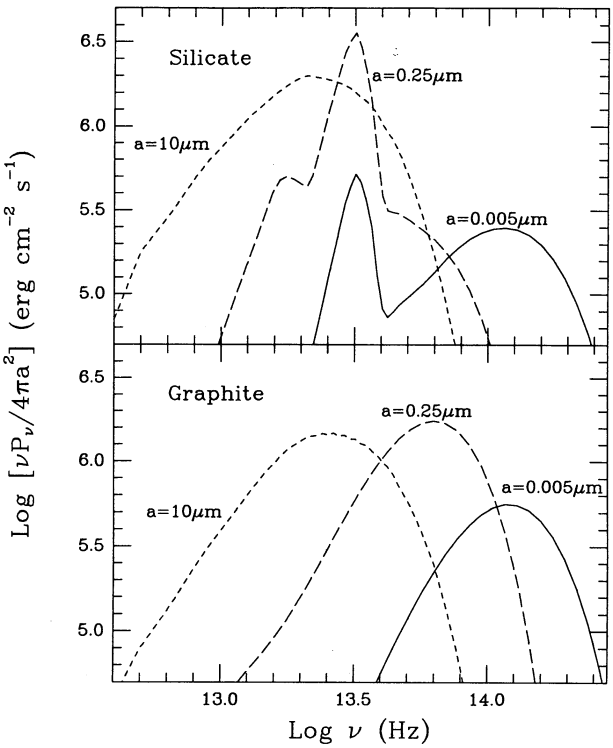

FIG. 9

FIG. 8.—Equilibrium temperature of silicate and graphite grains of various sizes as a function of their distance from the continuum source shown in Fig. 7. The horizontal lines at the upper left corner indicate the sublimation temperature of graphite and silicate grains. Note that the 0.005 μm silicate grains sublime at a distance which is larger by a factor of 20, compared with the 0.25 μm graphite grains. The grain temperature decreases, at any given distance, with increasing grain size, and spans a factor of 4–5 between 0.005 and 10 μm.

FIG. 9.—Emission per unit grain area from silicate and graphite grains at a distance of 5 pc from the continuum source shown in Fig. 7. The large range of spectral shapes results from the different grain equilibrium temperatures and emissivities. It demonstrates the large possible systematic error if only one grain size is used to calculate the dust emission. Note that the silicate feature disappears when $a = 10$ μm as expected given its $Q_{abs}(\nu)$.

The absorption efficiency, $Q^i_{abs}(a, \nu)$, is assumed to be independent of T_i, and its value is calculated for $T_i = 300$ K. This approximation becomes invalid when considering large graphite grains at long wavelengths (see DL Fig. 4*b*), but will not affect our conclusions. The dust is assumed to be optically thin in the IR and no optical depth corrections are made for the observed luminosity. We also assume above that the gas which is associated with the dust is ionized to a large enough degree so that practically all of the ionizing flux is absorbed by the dust; the validity of this assumption is further discussed in § 5.

3.3. *Optically Thick Dust*

A possible alternative configuration for the dust is in clouds which are individually optically thick at 10 μm. Efstathiou & Rowan-Robinson (1990) and Pier & Krolik (1992) have explored the emission properties of an axially symmetric dust distribution around a central point source. They both found that the shape of the silicate feature depends critically on the model parameters, in particular the system's inclination, and they show that the silicate feature disappears only within a very small region of parameter space. These models, however, includes either a single grain type, of a single size, or a single "equivalent" grain. Their work apparently indicates that if a significant silicate feature, in either emission or absorption, is present in the emission from any local region it will also be present when summing the emission over the whole configuration.

Below we calculate the IR emission from an optically thick plane parallel dust slab. We pay particular attention to the dependence of the silicate feature on the various model parameters: continuum shape, optical depth, and the dust properties. We show that the amplitude of the calculated feature is generally larger than observational limits, and then look for the minimal set of modifications required to suppress the feature to the observed level. This detailed analysis is done at the expense of using a simplified slab geometry. We note, however, that any arbitrary configuration can be described as a set of plane-parallel slabs at different inclinations, provided the depth at which $\tau_{9.7\,\mu m} = 1$ is much smaller than the system dimensions. In the following discussion of the radiative transfer we ignore absorption by a gas phase which might be associated with the dust; the validity of this approximation is discussed in § 5.

3.3.1. *The Radiative Transfer Method*

We use an iterative scheme in which one starts from a cold dust slab, divided into layers in equal logarithmic steps in $\tau_{9.7\,\mu m}$. For each layer we calculate the direct flux absorbed in each grain size and type, the resulting equilibrium grain temperatures and the emission spectra. We integrate over all grains to get the dust emission per unit volume at each grid point in the slab. We then

© American Astronomical Society • Provided by the NASA Astrophysics Data System

1993ApJ...402..441L

integrate over the slab volume to get the diffuse IR radiation field at each point. This radiation field, together with the incident radiation, is then used to recalculate the grain heating rate and equilibrium temperature. This calculation is iterated until the temperature has converged to the required accuracy, typically $\sim 1\%$ within 20 iterations. The observed flux at any angle is then obtained by integrating the emission from all layers. This method is not sensitive to the specific form of the initial guess for the temperature distribution, and proved to be robust as it converged for all cases we tested. The converged solution should satisfy energy conservation, i.e., the total power absorbed per unit area must equal the total emitted power. In the calculations below we assume the dust density is constant; the results are, however, independent of the density profile inside the slab, as long as the surface of constant density are parallel to the slab surface. This method can be generalized to any arbitrary geometry, as further discussed below.

3.3.2. *The Transfer of the Incident Flux*

We solve for the case of a plane parallel slab extending from $z = 0$ to $z = z_0$, divided into n layers of width Δz_j. Unlike the "optically thin" spherically symmetric dust distribution discussed above, here scatterings have a significant contribution to the extinction. The scattering phase function is approximated as being composed of a forward δ function component and an isotropic component. Since forward scattering has no effect, this approximation allows us to treat the scattering as isotropic with a cross section $\pi a^2(1 - g)Q^i_{\rm sca}(a, \nu)$. The extinction coefficient is then given by equation (24) where

$$Q^i_{\rm ext}(a, \nu) = Q^i_{\rm abs}(a, \nu) + (1 - g)Q^i_{\rm sca}(a, \nu) . \tag{30}$$

The slab is illuminated by a radiation field with a specific intensity $I^*_\nu(\mu, \phi)$, given in equation (25). Let $F_\nu(z_j) = cu_\nu(z_j)$ where $u_\nu(z_j)$ is the specific energy density of the radiation field at z_j. The contribution to $F_\nu(z_j)$ in a layer within $z_j - \Delta z_j/2$, to $z_j + \Delta z_j/2$ from the surface of the slab from the radiation incident on the slab is given by

$$F^*_{0,\nu}(z_j) = 2\pi c^j_\nu \int_0^1 I^*_\nu(\mu) e^{-\tau_\nu j/\mu} d\mu , \tag{31}$$

where $\tau^j_\nu = \alpha^{\rm ext}_\nu z_j$, and $\alpha^{\rm ext}_\nu$ is independent of z. The dimensionless correction coefficients

$$c^j_\nu \equiv \frac{e^{\Delta\tau_\nu j/2} - e^{-\Delta\tau_\nu j/2}}{\Delta\tau^j_\nu} , \tag{32}$$

where $\Delta\tau^j_\nu = \alpha^{\rm ext}_\nu \Delta z_j$, are introduced since the condition $\Delta\tau^j_\nu \ll 1$ cannot be maintained for all ν and j in a typical numerical realization. The power absorbed in a grain due to the incident flux is

$$P^{*,i}_{\rm abs}(a, z_j) = \pi a^2 \int_0^\infty Q^i_{\rm abs}(a, \nu) F^*_{0,\nu}(z_j) d\nu . \tag{33}$$

Some of the incident radiation is scattered, rather than absorbed. A fraction of the scattered radiation is able to escape outside the slab, and the rest either gets absorbed or is re-scattered. Below we describe how the transfer of the scattered flux is followed. The specific power scattered isotropically by a grain is

$$P^{*,i}_{{\rm sca},1,\nu}(a, z_j) = \pi a^2(1 - g)Q^i_{\rm sca}(a, \nu) F^*_{0,\nu}(z_j) , \tag{34}$$

where the suffix "1" stands for singly scattered photons. The singly scattered specific power per unit area from the whole layer centered at z_j is given by summing the contributions of all grains in the layer

$$G^*_{1,\nu}(z_j) = \Delta z_j \int_{a_{\rm min}}^{a_{\rm max}} \left[\sum_i P^{*,i}_{{\rm sca},1,\nu}(a, z_j) \frac{dn_i}{dn_i} \right] da . \tag{35}$$

Each layer is a source of scattered flux, which is further scattered and absorbed by all other layers. In the appendix we derive a set of coupling coefficients, $C^{j,k}_\nu$, which relate the specific power emitted or scattered by layer j to the incident specific power in layer k. Given these coefficients the specific power incident on a grain at z_j due to the scattered radiation from all other grains in the slab is

$$F^*_{1,\nu}(z_j) = \sum_{k=1}^{n} C^{j,k}_\nu G^*_{1,\nu}(z_k) . \tag{36}$$

The power absorbed from the singly scattered flux is

$$P^{*,i}_{{\rm abs},1}(a, z_j) = \pi a^2 \int_0^\infty Q^i_{\rm abs}(a, \nu) F^*_{1,\nu}(z_j) d\nu . \tag{37}$$

A fraction $(1 - g)Q^i_{\rm sca}(a, \nu)$ of the incident $F^*_{1,\nu}(z_j)$ is rescattered. One can generally express the specific power in n-times-scattered photons leaving a grain of type i as

$$P^{*,i}_{{\rm sca},n,\nu}(a, z_j) = \pi a^2(1 - g)Q^i_{\rm sca}(a, \nu) F^*_{n-1,\nu}(z_j) . \tag{38}$$

The amplitude of $P^{*,i}_{{\rm sca},n,\nu}(a, z_j)$ falls rapidly with increasing n and only a few iterations are required. The total power absorbed in each grain is obtained by summing the power absorbed over all orders of scattering and adding the power directly absorbed from the incident radiation, i.e.,

$$P^{*,i}_{\rm abs}(a, z_j) = \sum_{n=0}^{\infty} P^{*,i}_{{\rm abs},n} , \tag{39}$$

© American Astronomical Society • Provided by the NASA Astrophysics Data System

1993ApJ...402..441L

and the total specific scattered power from each grain is given by

$$P^{*,i}_{\mathrm{sca},\nu}(a, z_j) = \sum_{n=1}^{\infty} P^{*,i}_{\mathrm{sca},n,\nu}(a, z_j) . \tag{40}$$

This completes the transfer of the incident radiation $I^*_\nu(\mu)$. Below we describe how the transfer of the thermally reradiated flux is calculated.

3.3.3. *The Transfer of the Reradiated Flux*

The total flux absorbed in each grain directly and through repeated scatterings, $P^{*,i}_{\mathrm{abs}}(a, z_j)$, is reradiated in the IR. The grain equilibrium temperature, $T_i(a, z_j)$, is obtained, as in the "optically thin" case, by equating the heating and cooling rates,

$$P^{*,i}_{\mathrm{abs}}(a, z_j) = \int_0^{\infty} P^{i}_{\mathrm{em},\nu}(a, z_j) d\nu , \tag{41}$$

where

$$P^{i}_{\mathrm{em},\nu}(a, z_j) = 4\pi^2 a^2 B_\nu[T_i(a, z_j)] Q^i_{\mathrm{abs}}(a, \nu) , \tag{42}$$

and the contributions of all grains are summed to obtain the integrated thermal emission from the layer,

$$G_{0,\nu}(z_j) = \Delta z_j \int_{a_{\min}}^{a_{\max}} \left[\sum_i P^{*,i}_{\mathrm{em},\nu}(a, z_j) \frac{dn_i}{da} \right] da . \tag{43}$$

The iteration process followed now is similar to the one described for the scattering. The diffuse IR specific power incident on a grain at z_j due to the thermal emission of all other grains in the slab is

$$F_{0,\nu}(z_j) = \sum_{k=1}^{n} C^{j,k}_\nu G_{0,\nu}(z_k) . \tag{44}$$

A fraction of this flux is absorbed, and the integral over frequency, as in equation (33) gives the power absorbed due to self emission $P^i_{\mathrm{abs},0}(a, z_j)$. Note that IR scattering is often considered to be negligible and is usually not taken into account in the radiative transfer; here, however, we consider very large grains and therefore cannot neglect this process.

The IR scattered flux is followed using the same procedure described above for the scattering of the incident flux. The specific power in the n-scattered IR radiation, $P^i_{\mathrm{sca},n,\nu}(a, z_j)$ is calculated as in equation (38) and summed, as in equation (35), to give $G_{n,\nu}(z_j)$, which is then summed as in equation (36) to give $F_{n,\nu}(z_j)$. We thus obtain a rapidly converging series for the total power which is calculated as in equation (37). The total power absorbed from the dust-emitted IR radiation:

$$P^i_{\mathrm{abs}}(a, z_j) = \sum_{n=0}^{\infty} P^i_{\mathrm{abs},n} , \tag{45}$$

where $P^i_{\mathrm{abs},n}(a, z_j)$ is the power absorbed from n-scattered dust-emitted IR photons, calculated from $F_{n,\nu}(z_j)$ as in equation (37). The total specific power in scattered-dust–emitted radiation is given by

$$P^i_{\mathrm{sca},\nu}(a, z_j) = \sum_{n=1}^{\infty} P^i_{\mathrm{sca},n,\nu}(a, z_j) = \pi a^2 (1 - g) Q^i_{\mathrm{sca}}(a, \nu) \sum_{n=1}^{\infty} F_{n-1,\nu}(z_j) . \tag{46}$$

The quantity $P^i_{\mathrm{abs}}(a, z_j)$ is then added to the total power absorbed from the incident radiation, $P^{*,i}_{\mathrm{abs}}(a, z_j)$, to obtain a revised value for the total grain heating rate. The revised grain equilibrium temperature is then determined from

$$P^{*,i}_{\mathrm{abs}}(a, z_j) + P^i_{\mathrm{abs}}(a, z_j) = 4\pi^2 a^2 \int_0^{\infty} B_\nu[T_i(a, z_j)] Q^i_{\mathrm{abs}}(a, \nu) d\nu . \tag{47}$$

The revised value for the grain specific emitted power, $P^i_{\mathrm{em},\nu}(a, z_j)$, is now used to calculate the revised value of all other quantities in equations (43)–(46), and this process is iterated until $P^i_{\mathrm{em},\nu}(a, z_j)$ has converged to the required accuracy. The observed surface brightness of the slab is finally given by

$$I^{\mathrm{obs}}_\nu(\mu_{\mathrm{obs}}) = \frac{1}{4\pi\mu_{\mathrm{obs}}} \sum_{j=1}^{n} c^j_\nu \Delta z_j e^{-\tau_\nu j/\mu_{\mathrm{obs}}} \int_{a_{\min}}^{a_{\max}} \left[\sum_i P^i_{\mathrm{tot},\nu}(a, z_j) \frac{dn_i}{da} \right] da , \tag{48}$$

where $\mu_{\mathrm{obs}} = \cos\theta_{\mathrm{obs}}$, and

$$P^i_{\mathrm{tot},\nu}(a, z_j) = P^{*,i}_{\mathrm{sca},\nu}(a, z_j) + P^i_{\mathrm{sca},\nu}(a, z_j) + 4\pi^2 a^2 B_\nu[T_i(a, z_j)] Q^i_{\mathrm{abs}}(a, \nu) . \tag{49}$$

Energy conservation is implicitly built into the formalism described above, allowing an overall test for the FORTRAN implementation. Energy conservation was explicitly tested by comparing the incident to the outgoing power per unit area from both faces of the slab, i.e., by verifying that,

$$\int_0^{2\pi} d\phi \int_{-1}^{1} \mu\, d\mu \int_0^{\infty} I^*_\nu(\mu, \phi) d\nu = \int_0^{2\pi} d\phi \int_{-1}^{1} \mu_{\mathrm{obs}}\, d\mu_{\mathrm{obs}} \int_0^{\infty} I^{\mathrm{obs}}_\nu(\mu) d\nu , \tag{50}$$

is valid to the expected level of accuracy of about 1%.

© American Astronomical Society • Provided by the NASA Astrophysics Data System

1993ApJ...402..441L

The solution converges rather slowly at large optical depths. To accelerate the convergence we have at each iteration step multiplied the total emission from each layer by a single correction factor given by the ratio of the incident to outgoing power per unit area, and then calculated the resulting grain equilibrium temperature. These correction factors become very close to unity as the solution converges. In a more efficient method this factor would vary with grain size and position in the slab; our simple acceleration scheme, however, proved adequate for the slab geometry used here.

The details of the geometry of the dust configuration enter only through the values of the coupling coefficients, $C_\nu^{j,k}$. The iteration method described above can thus be applied to any arbitrary geometry once its coupling coefficients have been calculated. The computation time increases somewhat more rapidly than n^2, where n is the number of cells, thereby limiting its practical use to systems with at least some form of symmetry.

Below we explore in detail how the slab IR emission, and in particular the amplitude of the silicate feature, depend on the spectral shape of the incident radiation field, on the slab optical depth and orientation, and on the dust properties.

4. RESULTS

All calculations were carried out using either a graphite + silicate or a graphite + SiC grain mixture, 16 grain sizes spaced in equal logarithmic steps from 0.005 to 0.25 μm, 14 grain sizes in equal logarithmic steps from 0.332 to 10 μm, and 128 frequency bins unequally spaced from 1000 μm to 1 Å. We used 100 radial zones for the "optically thin" case, and 100 logarithmically spaced layers for the optically thick slab, and integrated the total slab emission using 100 angles equally spaced in μ from 1 to -1.

4.1. "*Optically Thin*" *Dust*

4.1.1. *MRN and Graphite* + SiC *Dust*

We first consider the cases of "MRN dust" (graphite + silicate, $\beta = -3.5$, 0.005 μm $\leq a \leq$ 0.25 μm, $A_{\rm sil}/A_{\rm gra} = 1.12$), and of dust composed of graphite + SiC grains with the same size distribution (but with $A_{\rm SiC}/A_{\rm gra} = 0.23$). Figure 10 displays the spectrum of a spherically symmetric dust distribution with $r_{\rm in} = 3L_{46}^{1/2}$ pc, $r_{\rm out} = 3L_{46}^{1/2}$ kpc, a radial density distribution with $\gamma = -1$, and an optical depth $\tau_{1200\,\text{Å}} = 0.5$, which corresponds to $E(B-V) = 0.033$ for the graphite + silicate mixture. The incident continuum was assumed to have a slope of -0.35 at $\lambda > 1250$ Å, which results in a transmitted continuum with a slope of ~ -0.5, i.e., similar to the value assumed for the observed slope (Fig. 7). The value of $r_{\rm out}$ is estimated from the long wavelength spectral steepening at $\lambda \sim 20$–50 μm (Fig. 7), and $\gamma = -1$ is determined by the requirement that the overall spectral slope in the 3–30 μm range is roughly -1. The column density, $N_{\rm H}$, is adjusted so that the total IR luminosity is similar to that of the "standard" AGN.

The flux of the MRN dust at 3 and at 30 μm can be approximately fitted to the observed continuum flux (as shown in Fig. 10), but the strong silicate feature at 9.7 μm is clearly inconsistent. Observations typically show no emission feature down to a level of about 30%–50%, or better in a few cases, while the calculated IR flux increases by a factor of 2.5 from 7.5 to 9.7 μm. A somewhat stronger feature is produced by SiC in the graphite + SiC dust mixture. Note that the shape of the SiC feature strongly depends on the grain shape (see Bohren & Huffman 1983), and it might be significantly broadened when a large range of shapes are present. Recall, however, that our adjusted dielectric function for SiC has already greatly broadened this resonance compared to crystalline specimens.

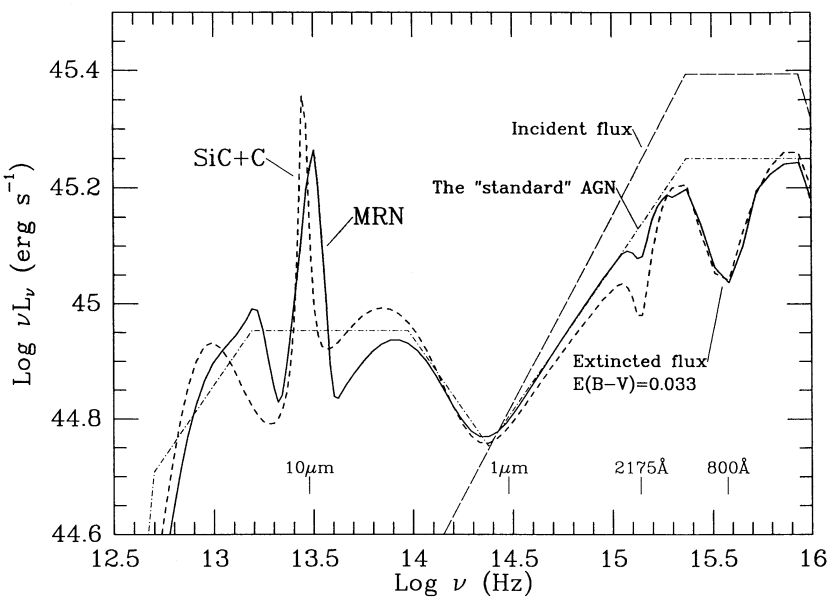

FIG. 10.—Emission of a spherical shell of MRN or a graphite + SiC dust with $\tau_{1200\,\text{Å}} = 0.5$ [$E(B-V) = 0.033$], $r_{\rm in} = 3.5$ pc, $r_{\rm out} = 3.5$ kpc and $\gamma = -1.1$. The incident continuum has a slope of -0.35 at $\lambda > 1250$ Å, which is reddened to the observed slope of -0.5 after transmission. The large absorption trough at $\lambda \sim 800$ Å results from the MRN dust absorption peak. The typical observed continuum is also shown. Note the very prominent silicate and SiC emission feature, such a feature has never been observed.

© American Astronomical Society • Provided by the NASA Astrophysics Data System

1993ApJ...402..441L

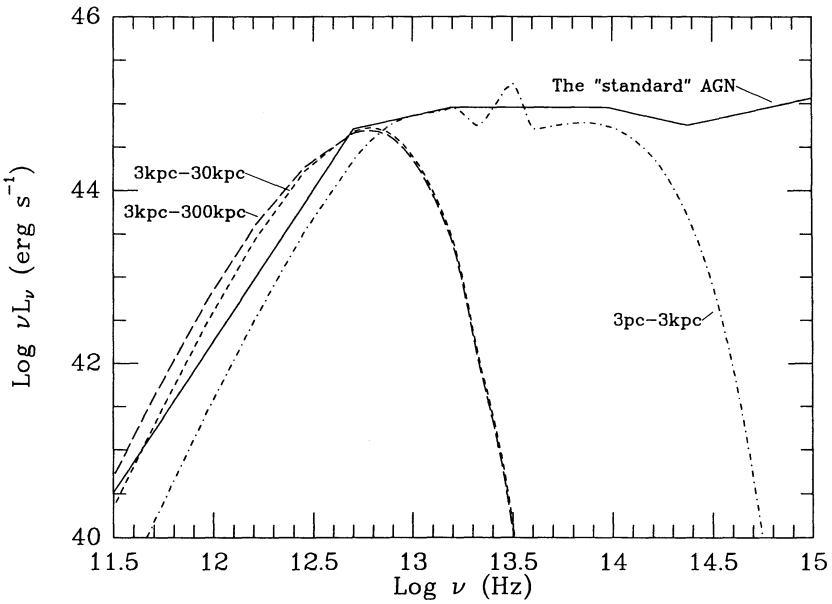

FIG. 11.—Long wavelength emission of the MRN dust model shown in Fig. 10, together with additional "galactic scale" dust at $r > 3$ kpc. The radial distance range of each component is indicated in the plot. The $r > 3$ kpc dust has a radial distribution with $\gamma = -2$ and $\tau_{1200\,\text{Å}} = 0.1$. The solid line is the assumed "standard" AGN continuum shape (Fig. 7), which has a slope of 2.5 at $\lambda > 60$ μm.

The optical-UV continuum is noticeably reddened, and two features are apparent; a small absorption trough at $\lambda \sim 2175$ Å with an amplitude of about 13% for "MRN dust", and a very pronounced absorption feature around 800 Å (16 eV). Note that this feature is (coincidentally) contributed to by both the small graphite grains (cf. Fig. 2) and the small silicate grains (cf. Fig. 3). The shape of the intrinsic continuum of AGNs generally cannot be determined to the required level of accuracy at $\lambda \sim 2175$ Å mainly due to the presence of broad unresolved emission components which cannot be clearly separated from the underlying continuum (e.g., Fig. 7 in Francis et al. 1991). The wavelength range of $\lambda \leq 800$ Å has been observed only in high redshift quasars, it is strongly affected by intervening unresolved Lyα absorption systems, and no definite conclusion concerning its presence can be obtained yet. The dust absorption features and reddening effect will not necessarily be present on all lines of sight if the dust covers less than 4π of the central continuum source. The dust IR emission is however isotropic, and the absence of the predicted strong emission features near 10 μm clearly rules out thermal emission from warm MRN or a graphite + SiC dust in any configuration which is optically thin at 10 μm.

Figure 11 displays the long wavelength emission of the MRN dust model shown in Figure 10, together with a Galactic scale MRN dust component with $\gamma = -2$ and $\tau_{1200\,\text{Å}} = 0.1$ [$E(B-V) = 0.0066$] extending from $3L_{46}^{1/2}$ kpc to either $30L_{46}^{1/2}$ kpc or $300L_{46}^{1/2}$ kpc. The optical depth, $\tau_{1200\,\text{Å}} = 0.1$, corresponds to a column density of H nuclei, $N_{\text{H}} = 8.9 \times 10^{19}$ cm^{-2}, and a total mass of 7.5×10^8 $M_\odot$ or 7.5×10^9 $M_\odot$. Available data on the continuum of radio-quiet AGNs in the mm–sub-mm wavelength range is rather scarce; in those few objects where detections were made a power-law index of $\sim$2.5 or steeper, between 100 μm and 1.3 mm, is indicated (Chini, Kreysa, & Biermann 1989). The corresponding slopes in the two models shown in Figure 11 are 3.1 and 2.8, respectively. These values are significantly flatter than the slope of 4 expected from "optically thin" dust emitting at the Rayleigh-Jeans regime, but are somewhat steeper than in the few cases where this slope is observationally determined. One should note however that the observed slopes may be affected by significant free-free or nonthermal radio emission which is usually observed in the cm range.

Below we explore various modifications to the MRN dust which can significantly reduce the amplitude of the silicate emission feature. We do not discuss in detail the case of graphite + SiC dust as it will be subject to qualitatively similar constraints.

4.1.2. *Modified Composition*

A simple solution for the absence of a prominent silicate feature is obtained if silicate grains are preferentially depleted. Figure 12 presents the spectrum from grains with the MRN size distribution with silicates depleted to various levels, with $\tau_{1200\,\text{Å}} = 0.4$. A depletion to 20% of the MRN value (i.e., $A_{\text{sil}}/A_{\text{gra}} = 0.22$) reduces the feature amplitude to 31%, where the feature amplitude is defined here, for practical purposes, as $(\nu F_\nu)_{9.7\,\mu\text{m}}/(\nu F_\nu)_{7.5\,\mu\text{m}} - 1$. With $A_{\text{sil}}/A_{\text{gra}} = 0.11$ the feature is reduced to 9.7%, which is well below current observational limits. The calculated IR continuum also has broad maxima around 5 μm and 30 μm. Some objects do seem to show a broad emission bump around 3–5 μm (e.g., Edelson & Malkan 1987), but most are consistent with a featureless continuum. The data quality at $\lambda > 10$ μm, mostly very broad-band *IRAS* photometry, is not yet high enough to reveal the presence of the predicted continuum features at the level shown. We also note that these broad features are subject to some theoretical uncertainty present in the optical properties of graphite grains in this wavelength range (see DL).

The 2175 Å absorption feature, produced by the small graphite grains ($a \leq 0.04$ μm), is stronger than the one produced in the case of the normal MRN dust (Fig. 10). This feature will, however, not be observable if dust is not present along the line of sight. It will also be absent if small graphite grains ($a < 0.04$ μm) are preferentially destroyed.

© American Astronomical Society • Provided by the NASA Astrophysics Data System

1993ApJ...402..441L

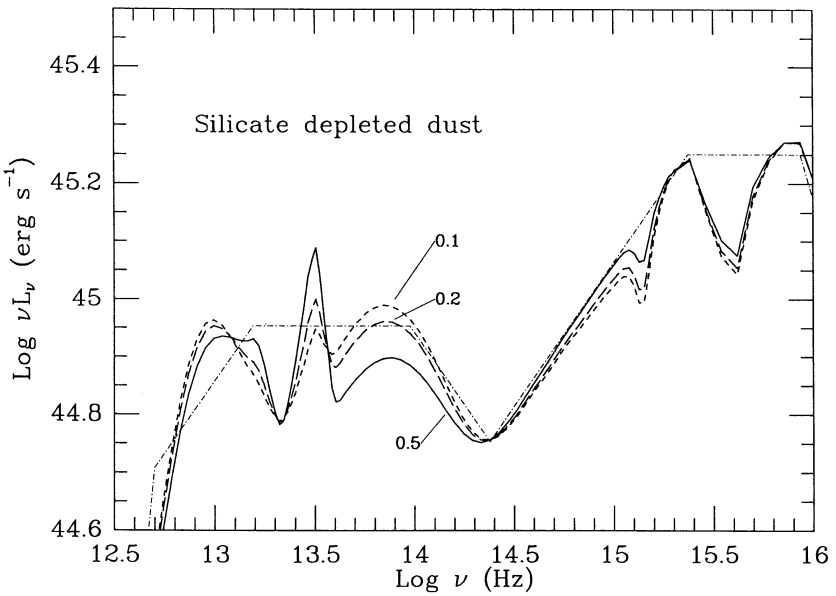

FIG. 12.—Same as in Fig. 10 for MRN-like silicate depleted dust. The fractional abundance of silicates relative to the MRN abundance is indicated near each curve. In all cases shown $\tau_{1200\,\text{Å}} = 0.4$, $r_{in} = 3$ pc, $r_{out} = 3$ kpc and $\gamma = -1$. Note that the 2175 Å absorption trough increases when the silicates get more depleted, due to the increased contribution of small graphite grains to the absorption. At a depletion of 0.2 the silicate feature amplitude is within the measurement error for most object. The deep at 20 μm is subject to some uncertainty present in the dielectric function of realistic graphite grains.

4.1.3. *Modified Size Distribution*

As shown in § 2 the amplitude of the silicate feature of individual grains decreases in grains with $a \geq 3$ μm (Fig. 5). We therefore expect dust in which such very large grains are abundant to have a weaker emission feature.

Figure 13 presents the continuum emission of dust with a grain size distribution which extends to $a_{max} = 10$ μm, with different values for the grain size distribution exponent, β. For $\beta = -3.5$ we require $\tau_{1200\,\text{Å}} = 0.5$; for $\beta = -2.5$ and $\beta = -1.5$ we take $\tau_{1200\,\text{Å}} = 0.35$. Note that when $\beta = -3.5$ the silicate feature amplitude is still 150%; this occurs since most of the grain surface area, and hence most of the energy absorption and reemission, lies at the small end of the grain size distribution. When $\beta = -2.5$ the grain surface area is dominated by the largest grains, and the amplitude of the emission feature falls to 39%, and when $\beta = -1.5$ the

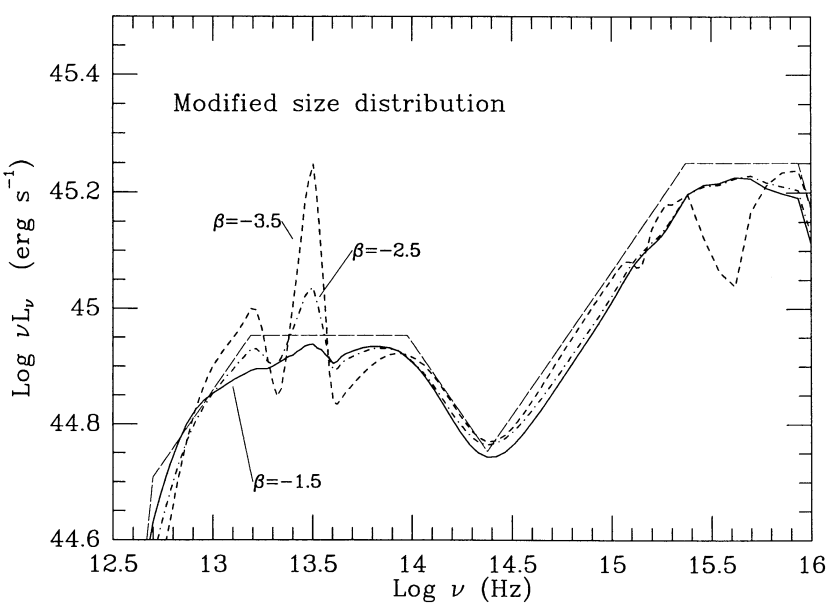

FIG. 13.—Same as in Fig. 10 for dust with various size distributions. In all cases the grain size distribution extends to $a_{max} = 10$ μm, and β (see text) is indicated near each curve. In the cases of $\beta = -2.5, -1.5$ the absorption is almost featureless, and the incident continuum was assumed to have a power-law slope of -0.5 at $\lambda < 1250$ Å. The amplitude of the silicate feature becomes marginally consistent with the observational limits at $\beta = -2.5$. Note that the dust radial extent is strongly dependent on the specific dust model assumed (see Table 2).

© American Astronomical Society • Provided by the NASA Astrophysics Data System

1993ApJ...402..441L

TABLE 2

MODELS OF "OPTICALLY THIN" DUST WITH A REDUCED SILICATE FEATURE

Model	$\tau_{1200\,\text{Å}}/N_{\text{H}}$ (10^{-24} cm^2)	N_{H} (10^{20} cm^{-2})	r_{in} ($L_{46}^{1/2}$ pc)	r_{out} ($L_{46}^{1/2}$ pc)	M_{H} ($10^6 L_{46}\,M_\odot$)	$n_{\text{H}}(r_{\text{in}})$ ($L_{46}^{-1/2}$ cm^{-3})	$n_{\text{H}}(r_{\text{out}})$ ($L_{46}^{-1/2}$ cm^{-3})	σ_{pr} (10^{-24} cm^2)
A	1060	3.77	3	3000	23	6	0.006	1043
B	1110	3.60	3	3000	22	6	0.006	1096
C	9.06	386	0.3	300	8.7	4300	2	12.48
D	4.74	738	0.2	200	7.3	12000	6	7.16

NOTES.—Model A: MRN size distribution, silicates depleted to 20%, $\gamma = -1$. Model B: MRN size distribution, silicates depleted to 10%, $\gamma = -1$. Model C: $a_{\text{max}} = 10\,\mu\text{m}$, $\beta = -2.5, \gamma = -1.1$. Model D: $a_{\text{max}} = 10\,\mu\text{m}$, $\beta = -1.5, \gamma = -1.1$.

feature amplitude reduces to only 8%. The dust models with $\beta = -2.5$ and -1.5 have gray extinction curves, the dust has no reddening effect in the optical and UV, and the incident continuum slope at $\lambda < 1250$ Å was therefore assumed to be $\alpha = -0.5$.

As shown above large grains have a significantly lower temperature at most distances compared with normal grains (Fig. 8), and the 3–30 μm emission is therefore emitted at distances which are about a factor of 10 smaller for $\beta = -2.5$ and -1.5 (see Table 2). We note that the grain size distribution in fact changes with distance due to evaporation of small grains when r decreases below a few pc. This effect was taken into account when calculating the grain emission in models C and D (Table 2), but was neglected in the calculation of the dust optical depth (left-hand side of eq. [25]). This results in a very small correction to the dust extinction in models C and D since most of the opacity is produced by the largest grains.

In Table 2 we give the parameters of various modified dust models in which the silicate emission feature is significantly reduced. Dust dominated by large grains has an absorption opacity in the UV which is lower by two orders of magnitudes than that of the MRN dust (Fig. 6), it therefore requires a correspondingly higher gas column density to obtain a given τ_ν. However the total implied gas mass (§ 5.1) turns out to be somewhat smaller than for MRN dust (Table 2) since the higher column density is coincidentally compensated by the order of magnitude decrease in the dust distance. Observational constraints on the presence of such gas near the center of AGNs are discussed in § 5.

4.2. *Optically Thick Dust*

4.2.1. *Graphite + Silicate and Graphite + SiC Dust*

The slab spectrum is uniquely determined once the temperature profiles of all grain species inside the slab are known. Figure 14*a* compares the temperature profiles of silicate grains inside a slab made of "MRN dust" when the incident flux is the only heating source taken into account, and when self-heating by the diffuse IR radiation field from all other grains is also taken into account. Close to the surface self-heating has a small effect on the temperature of large grains, and no noticeable effect on the temperature of small grains, as these absorb the diffuse IR flux with a much lower efficiency. At large optical depths the incident IR has some heating effect, but most of the heating is through the transfer of the thermal emission of grains near the surface. Note that all grains reach the same tempetature at a large enough optical depth. This occurs when $Q_{\text{abs}}(a, \nu)$ can be expressed in the separable form $f(a)g(\nu)$, which occurs when $\lambda \gg a$, or, alternatively, when the grains are embedded in a blackbody radiation field. The dependence of the temperature profile on the slab inclination, μ_{in}, is shown in Figure 14*b*; in all cases the temperature of the uppermost, optically thin, part of the slab is essentially the same, but the depth of the hot layer is strongly dependent on the inclination of the slab.

We consider a slab of area A at a distance d from the continuum source. The apparent luminosity of the slab as seen by a distant observer is

$$l_\nu^{\text{app}}(\mu_{\text{obs}}) \equiv 4\pi A \mu_{\text{obs}} I_\nu(\mu_{\text{obs}}) \,. \tag{51}$$

Figure 15 presents $L_\nu^{\text{app}}(\mu_{\text{obs}}) \equiv l_\nu^{\text{app}}(\mu_{\text{obs}})[4\pi d^2/A]$ for a slab with $\tau_{9.7\,\mu\text{m}} = 20$ for various values of μ_{obs} and μ_{in}. The slab is at a distance $d = 5L_{46}^{1/2}$ pc, at which its peak emission is around 10 μm. At each value of μ_{in} the slab spectrum gets softer as μ_{obs} increases since more emission from the deeper, cooler, layers is able to escape. The near-IR flux does not vary much with inclination as most of it is produced in a very thin hot layer at the top of the slab which is nearly optically thin to its thermal emission. The slab spectrum gets colder as the inclination, with respect to the continuum source, increases since the flux absorbed per unit slab area decreases. The total power emitted is not directly proportional to μ_{in} since there is a fixed contribution from the semi-isotropic IR flux at $\lambda > 1.2$ μm. The amplitude of the silicate feature is significantly smaller at small μ_{in}, due to the dominance of the incident isotropic IR flux at low inclinations, as further demonstrated below.

The dependence of the silicate feature amplitude on the optical depth of the slab is displayed in Figure 16. The amplitude of the emission feature decreases with increasing optical depth and saturates at a level of 57% for $\tau_{9.7\,\mu\text{m}} > 10$. The intensity from the back side of the slab develops an absorption feature at 9.7 μm as the optical depth increases, but the intensity is low and cannot significantly affect the emission averaged over 4π. The presence of an emission feature in the angle averaged slab flux is therefore independent of its optical depth.

A direct comparison of the emission of "optically thin" and optically thick dust situated at the same distance from the center is shown in Figure 17 for both MRN and graphite + SiC compositions. The difference in the amplitudes of the silicate and the SiC features between the "optically thin" and thick cases are clear. Note also that the continuum of an "optically thin" dust model is significantly hotter, since most of the incident flux in the "optically thin" case is absorbed by the smallest grains which produce a relatively hot continuum, whereas in the optically thick case a significant part of the flux comes from the inner cooler parts of the slab.

© American Astronomical Society • Provided by the NASA Astrophysics Data System

1993ApJ...402..441L

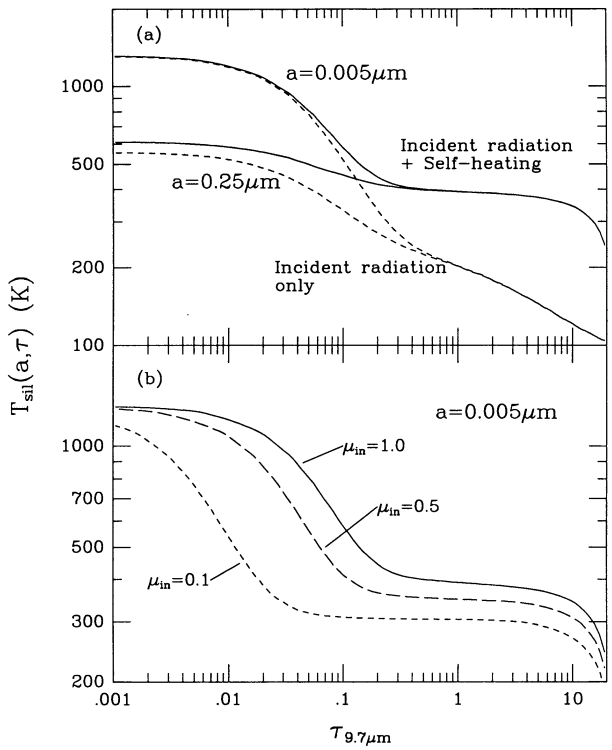

FIG. 14.—(*a*) Temperature profile of silicate grains with $a = 0.005$ and 0.25 μm as a function of optical depth inside a slab composed of a graphite + silicate MRN grain mixture. The slab is at a distance of 3 pc, and face-on ($\theta_{in} = 0$) to the continuum source (Fig. 7). The dashed curve displays the temperature when only the incident flux is taken into account (this provides the initial conditions for the iterative scheme described in the text). The solid curve displays the temperature when self-heating is taken into account. At large optical depths all the grains reach the same temperature and the diffuse radiation field becomes a blackbody. (*b*) Temperature profile of silicate grains with $a = 0.005$ inside a slab at different inclinations to the continuum source. The incident flux at $\lambda > 1.2$ μm in all cases is uniform over 2π. The temperature of the top layer, which is optically thin in the UV, is independent of inclination, but the depth of this layer varies with $\mu_{in}(=\cos\theta_{in})$.

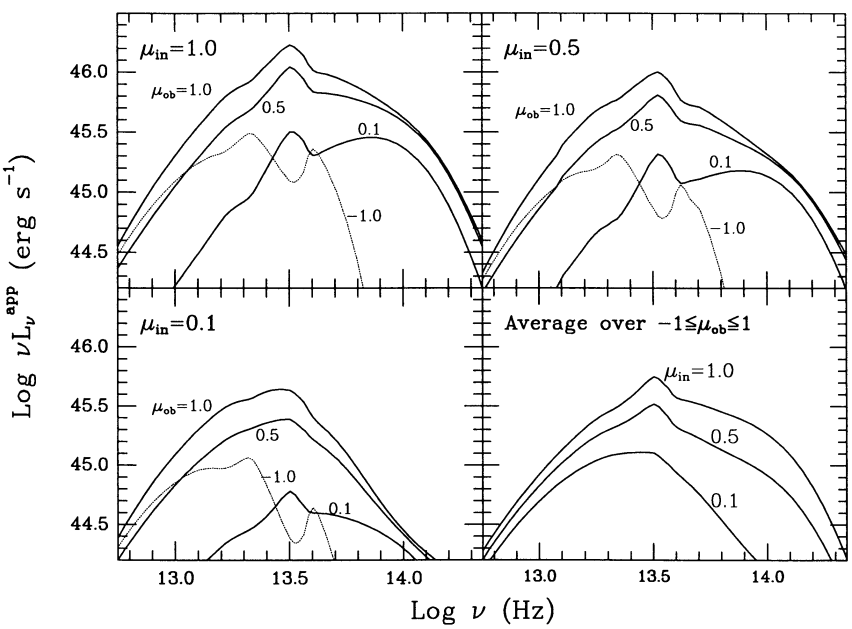

FIG. 15.—Emission of a slab with $\tau_{9.7\,\mu m} = 20$ at a distance of 5 pc from a continuum source (L_ν^{app} is defined in the text). The slab inclination angle with respect to the continuum source is indicated by μ_{in}. Each panel presents the observed continuum for three different inclinations of the slab with respect to the line of sight, μ_{ob}. The emission at 3 μm does not vary much with inclination (for $\mu_{ob} > 0$) since it is mostly emitted from a very thin layer heated directly by the incident UV flux which has a low optical depth at 3 μm. The lower right panel compares the slab emission averaged over 4π for different values of μ_{in}. The slab emission gets colder as the power absorbed per unit area decreases with decreasing μ_{in}.

© American Astronomical Society • Provided by the NASA Astrophysics Data System

1993ApJ...402..441L

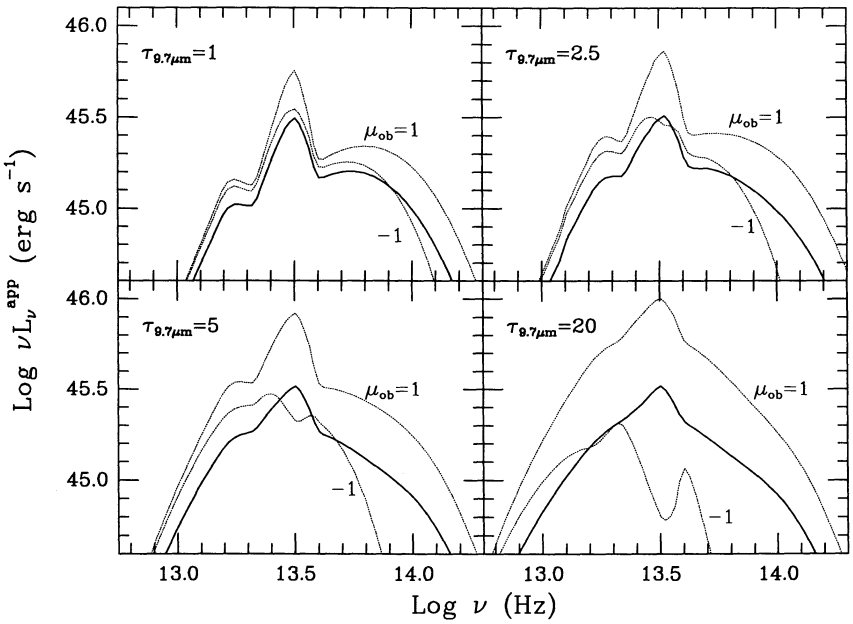

FIG. 16.—Emission of a slab composed of "MRN dust" at $\mu_{in} = 0.5$ and different values of $\tau_{9.7\,\mu m}$. The upper thin curve in each panel represents the observed emission for $\mu_{ob} = 1$, and the lower curve at $\mu_{ob} = -1$ (from the back side of the slab). The solid curve represents the emission averaged over 4π. As $\tau_{9.7\,\mu m}$ increases the emission from the back side develops a silicate absorption feature, but the amplitude of the flux drops and it cannot affect significantly the angle averaged emission. The amplitude of the silicate feature decreases with increasing $\tau_{9.7\,\mu m}$, and saturates for $\tau_{9.7\,\mu m} > 10$.

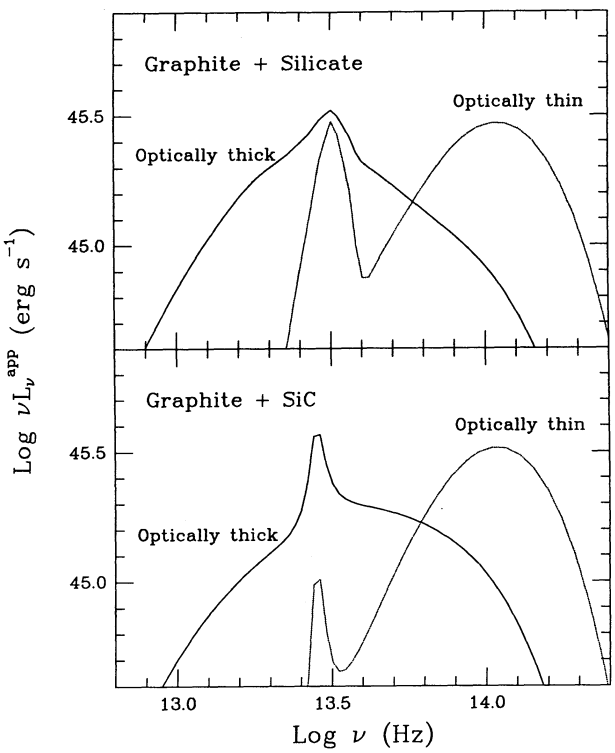

FIG. 17.—(*a*) Comparison of the emission from an "optically thin" and optically thick 'MRN dust", both situated at a distance of 5 pc from the continuum source. The parameters in the optically thick case are as in Fig. 16 with $\tau_{9.7\,\mu m} = 20$. The "optically thin" flux was scaled up to the same apparent bolometric luminosity. The continuum from the "optically thin" dust is significantly hotter since most of the emission originates from the smallest (hottest) grains. Note the large difference in the amplitude of the silicate emission feature. (*b*) Same as in Fig. 17*a* but for a graphite + SiC grain mixture with $A_{SiC}/A_{gra} = 0.23$.

© American Astronomical Society • Provided by the NASA Astrophysics Data System

1993ApJ...402..441L

The calculation of a slab spectrum at $r < 4L_{46}^{1/2}$ pc is complicated by the fact that the smallest grains evaporate at these distances. The radiative transfer must then take into account the fact that the grain size distribution and composition varies with depth inside the slab, as different grains sublime. This level of sophistication is beyond the scope of this paper, and the region at $r < 4L_{46}^{1/2}$ pc was avoided.

The results above indicate that a high optical depth in the IR can significantly suppress the silicate emission feature, although its amplitude is still large enough to be detectable in most objects. Below we study modifications of the dust properties and the incident radiation field which can affect the amplitude of the silicate feature.

4.2.2. *Possible Modifications*

The effect of silicate depletion is shown in Figure 18*a*. A depletion to 50% of their MRN value reduces the silicate feature amplitude from 57% to 39%, and a depletion to 20% reduces it to only 20%. The effect of a modified size distribution is shown in Figure 18*b*. Increasing a_{max} to 10 μm without changing the grain size distribution exponent (-3.5) reduces the feature amplitude to 53%. If in addition the power-law exponent is changed to -2.5 then the continuum becomes essentially featureless. The last result can be understood from the extinction curve which corresponds to this size distribution (Fig. 6): the extinction in the optical–UV is comparable to the one around 10 μm, thus the incident flux penetrates to a considerable optical depth at 9.7 μm, this results in a low temperature gradient in the 10 μm emitting region inside the slab, and as a result, a quasi-blackbody emission.

The dependence of the silicate feature on the energy distribution of the incident flux is shown in Figure 18*c*. When a spectral slope $d \ln L_\nu / d\nu = -0.35$ is extended for all $\lambda > 1250$ Å (the incident spectrum in Fig. 10) the fraction of IR flux in the incident radiation is reduced compared with the continuum shown in Figure 7. In this case almost all of the incident power is absorbed in a thin layer, a steeper temperature gradient is produced inside the slab, and a stronger emission feature (86%) results. When the incident flux is assumed to be a power law with a slope of -1 and a cutoff at $\lambda < 911.8$ Å the feature practically disappears. This occurs since most of the incident power is now in the IR, the slab is heated in a more uniform fashion, and approaches the case of an isothermal slab, in which the outgoing flux approaches a blackbody when the optical depth becomes large. A similar incident continuum shape was assumed by Pier & Krolik (1992) who obtained a silicate feature of a larger amplitude. These discrepant results might be due to their use of a single "equivalent" grain instead of taking a range of grain sizes and types as done here. Note that the continuum shape

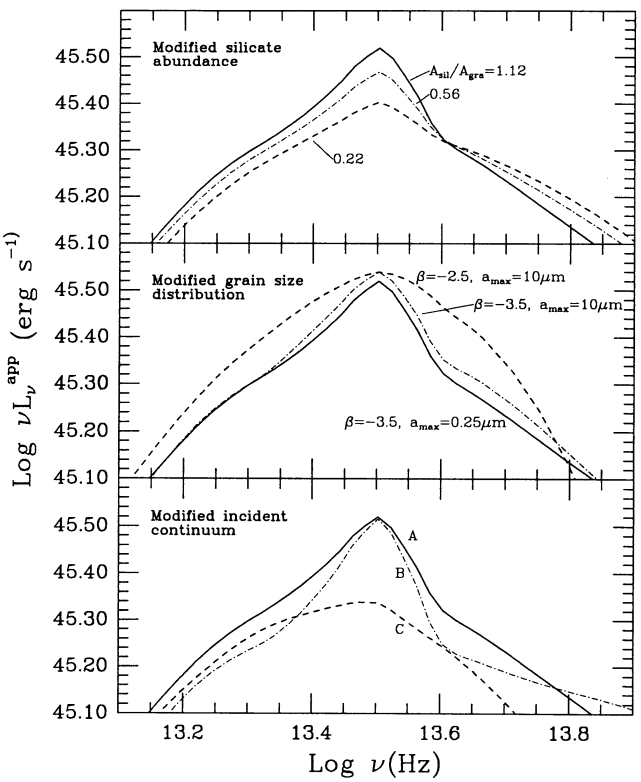

FIG. 18.—Dependence of the silicate feature amplitude from an optically thick slab on various model parameters. In all cases $r = 5$ pc, $\tau_{9.7\,\mu m} = 20$, $\mu_{in} = 0.5$, and the observed emission is averaged over 4π. *Upper panel:* Dependence on the silicate/graphite abundance. The value of A_{sil}/A_{gra} is indicated near each curve, where $A_{sil}/A_{gra} = 1.12$ is the MRN value. A depletion by a factor of 5 reduces the feature amplitude to well below the observational limit in most objects. *Middle panel:* Dependence on grain size distribution. The MRN distribution has $\beta = -3.5$, $a_{min} = 0.005$ μm and $a_{max} = 0.25$ μm, other distributions have $a_{min} = 0.005$ μm and other parameters as marked. The silicate emission feature completely disappears for $\beta = -2.5$ and $a_{max} = 10$ μm, this occurs since the extinction curve is flat (Fig. 6*a*), the incident flux penetrates to a large depth, which results in a very low temperature gradient inside the slab. *Lower panel:* Dependence on the energy distribution of the incident continuum. Curve A represents the result for the continuum shown in Fig. 7. Curve B, the result for the "dereddened" incident continuum shown in Fig. 10. In this case almost all of the heating is by UV radiation which penetrates only a small depth into the slab, produces a steeper temperature gradient, and a stronger emission feature. Curve C, the result for an incident continuum with a uniform power law slope of -1 and zero flux at $\lambda < 911.8$Å and $\lambda > 1000$ μm. In this case the heating is mostly by IR radiation which penetrates to a large depth, produces a small temperature gradient, and a very weak feature.

© American Astronomical Society • Provided by the NASA Astrophysics Data System

1993ApJ...402..441L

assumed in Figure 18*c* is generally unrealistic as the optical–UV emission is observed to have a rather different shape in most objects (e.g., Sanders et al. 1989).

Note that the IR energy distribution has no effect on the dust emission properties when the dust is "optically thin" (§ 4.1).

The results shown above indicate that the silicate feature can be effectively suppressed by modifications which are less radical compared with those required in the case of "optically thin" dust. Note that the amplitude of the silicate feature is determined by the temperature gradient inside the slab; if other heat sources are present inside the slab, as for example in the case of young stars embedded inside molecular clouds, then a lower temperature gradient will be formed, and the silicate amplitude will be suppressed.

5. CONSTRAINTS FROM THE ASSOCIATED GAS PHASE

The constraints derived above were based only on the dust emission. If the dust is associated with some gas (as usually expected) then the gas can also have observable effects. Below we discuss the associated gas opacity and line emission, assuming a dust to H mass ratio $f_d = 0.010$ for the graphite + silicate mixture, and $f_d = 0.0058$ for the graphite + SiC mixture.

5.1. *"Optically Thin" Dust*

We first estimate the total mass in the gas phase. Given a power law gas density distribution of the form given in equation (28) with a column density $N_{\rm H}$, then the gas mass is

$$M_{\rm H} = 4\pi r_{\rm in}^2 N_{\rm H} m_{\rm H} \left(\frac{1+\gamma}{3+\gamma}\right) \frac{(r_{\rm out}/r_{\rm in})^{\gamma+3} - 1}{(r_{\rm out}/r_{\rm in})^{\gamma+1} - 1} \qquad \text{for } \gamma \neq -1, -3 . \tag{52}$$

The column density, $r_{\rm in}$, $r_{\rm out}$ and γ were estimated in § 4.1.3, for different dust models, based on the typical AGN emission in the IR (Fig. 7). The masses deduced are given in Table 2. These masses should only serve as order of magnitude estimates for the gas associated with dust emitting in the 3–30 μm range.

Given the ionizing continuum incident on the dust (Fig. 7), we deduce the following values: the number of H ionizing photons is $\dot{N}_{\rm ion} = 6.6 \times 10^{55} L_{46}\ {\rm s}^{-1}$ (a value of $9.3 \times 10^{55} L_{46}\ {\rm s}^{-1}$ is obtained if the incident continuum is "dereddened" as shown in Fig. 10), the average ionizing photon energy, $\epsilon_{\rm av}$ is 2.75 ryd (=37.4 eV), and the H^0 absorption cross section averaged over all ionizing photons is $\sigma_{\rm av}^{\rm H^0} = 2.05 \times 10^{-18}\ {\rm cm}^{-2}$.

The ratio of ionized to neutral H, when photoionization is the only ionizing process, is given by

$$\frac{N_{\rm H^+}(r)}{n_{\rm H^0}(r)} = Uc \frac{\sigma_{\rm av}^{\rm H^0}}{\alpha_B} = 2.37 \times 10^5 U , \tag{53}$$

where $\alpha_B = 2.59 \times 10^{-13}\ {\rm cm}^3\ {\rm s}^{-1}$ is the case B recombination coefficient for H at 10^4 K (Osterbrock 1989). The ionization parameter, U, is defined by

$$U(r) \equiv \frac{\dot{N}_{\rm ion}}{4\pi c r^2 n_e} , \tag{54}$$

where $n_e(r)$ is the electron density, and $\dot{N}_{\rm ion}$ is assumed to be independent of r. The fractional ionization decreases with radius when $\gamma > -2$, but the absolute value of $U(r_{\rm out}) \gtrsim 100$ (for all models given in Table 2) is large enough to yield $n_{\rm H^0}(r)/n_{\rm H}(r) < 10^{-7}$ at all $r \leq r_{\rm out}$. The optical depth from $r_{\rm in}$ to $r_{\rm out}$ at $\lambda < 911.8$ Å to H^0 is therefore much smaller than unity. The gas phase opacity of heavier elements can be estimated using the calculations of Krolik & Kallman (1984) for the case of gas photoionized by a power-law continuum source; their results indicate that the high value $U(r)$ significantly reduces the gas opacity below 1 keV. The metals in the grains remain neutral, but their column density is modest: the optical depth just above the carbon K edge (284 eV) is only 12% in model A, and rises to 52% in model D, which is still below current detection limits. The optical depth of the gas to electron scattering is always smaller than 5%, and electron scattering would have no detectable effects.

The Lyα emission can be estimated assuming case B recombination from

$$\dot{N}_{\rm Ly\alpha} = \alpha_{\rm B} \int_{r_{\rm in}}^{r_{\rm out}} \langle n(r) \rangle^2 f^{-1} 4\pi r^2\, dr , \tag{55}$$

where $\langle n(r) \rangle$ is the locally averaged density at a distance r, and using the approximation $n(r) = n_e(r) = n_{\rm H^+}(r)$. The quantity f is the fractional volume filled by the gas. In all cases given in Table 2 the Lyα equivalent width, EW, is smaller by at least three orders of magnitude than the typical observed EW (~ 70 Å, e.g., Netzer 1990), unless the gas filling factor is much smaller than unity.

We therefore conclude that the gas phase associated with "optically thin" dust is not likely to have a pronounced observational effect. This gas might however emit some high ionization lines, as suggested by Korista & Ferland (1989) in the context of line emission from the interstellar medium of the host galaxy. Such lines, given a proper theoretical prediction, could be used to constrain the presence of "optically thin" dust.

5.2. *Optically Thick Dust*

The column density of a slab with MRN dust is given in terms of $\tau_{9.7\,\mu{\rm m}}$ by $N_{\rm H} = 3 \times 10^{22} \tau_{9.7\,\mu{\rm m}}\ {\rm cm}^{-2}$. A column density of $\sim 3 \times 10^{23}\ {\rm cm}^{-2}$ or larger is therefore required to significantly reduce the silicate feature amplitue, as shown in § 4.2. The observed ratio of $L_{\rm IR}$ to $L_{\rm bol}$ implies that the dust should have a covering factor $C \sim \frac{1}{3}$ or $\sim \frac{1}{2}$, depending on the specific geometry adopted. An estimate of $r_{\rm in}$ and $r_{\rm out}$ will allow us to get a lower limit on the gas mass. As mentioned in § 4.2 we did not calculate the spectrum from a slab at $r \lesssim 4 L_{46}^{1/2}$ pc, but we can estimate the range of radii required to reproduce the overall observed IR spectral shape using

© American Astronomical Society • Provided by the NASA Astrophysics Data System

1993ApJ...402..441L

the fact that the slab emission is colder than that of "optically thin" MRN dust, and resembles that of dust dominated by very large grains. Assuming $0.3L_{46}^{1/2}$ pc $< r < 0.3L_{46}^{1/2}$ kpc, $C \sim \frac{1}{3}$, and $\tau_{9.7\,\mu m} \geq 10$, we get $M_H > 6.7 \times 10^7 L_{46}\, M_\odot$

The gas inside a high column density cloud will be relatively cold and opaque: a slab with MRN dust and $\tau_{9.7\,\mu m} = 10$ becomes transparent only at $h\nu > 5$ keV. Thus if these clouds are larger than the continuum source they will either completely block the central continuum source, or have no effect at all, and if they are smaller than the central continuum source, they will produce a wavelength-independent absorption. The gas in the face of the cloud exposed to the continuum source is photoionized and is likely to cool mostly by line emission. The line flux can be very large since $C \sim \frac{1}{3}$–$\frac{1}{2}$. Below we estimate the expected Lyα flux and the constraints it imposes on the value of U. In contrast with dusty H II regions, where most of the Lyα photons are absorbed by dust before they are able to diffuse out, here the basic geometry is that of reflection rather than transmission (e.g., Neufeld 1991) and a significant fraction of the Lyα photons will escape. Studies of the radiative transfer of resonance lines (e.g., Hummer & Kunasz 1980; Neufeld 1990) indicate that the mean total path traversed by resonance scattering of a photon, emitted at an optical depth τ_0 (for a line-center photon) inside a semi-infinite slab, is of the order of τ_0. Thus if the probability of an ionizing photon to be absorbed by dust is significantly smaller than one, then the Lyα photon produced by recombination will also have a small probability to be extinguished by dust before it escapes from the photoionized surface of the cloud. The argument above assumes that σ^{dust}(1216 Å) $\lesssim \sigma^{dust}$(ionizing photon), which is true for most ionizing photons. Assuming one Lyα photon is emitted per absorption of an $h\nu > 13.6$ eV photon from the AGN (case B recombination), a covering factor of 33% will result in an EW of Lyα of 243 Å, for the "standard" AGN continuum. The observed EW is $\sim$70 Å, most of which is in a broad component, which is known from line variability time scales to be associated with clouds much closer to the center. We therefore conclude that the opacity at $\lambda < 911.8$ Å at the photoionized surface of the cloud must be dominated by the dust rather than the gas phase.

The lines emitted from clouds at a distance of the order of a few pc are likely to be narrow, i.e., FWHM $\lesssim 1000$ km s^{-1}. The narrow-line flux indicates that the narrow-line–producing gas absorbs only about 1%–2% of the ionizing continuum. Thus given optically thick clouds with a covering factor of $\sim\frac{1}{3}$ we require that less than 10% of the ionizing continuum incident on the high column density clouds should be directly absorbed in the gas phase, i.e.,

$$\sigma_{av}^{gas}/\sigma_{av}^{dust} < 0.1\ , \tag{56}$$

where

$$\sigma_{av}^{gas} = 2.05 \times 10^{-18} n_{H^0}/n_H\ \text{cm}^2\ , \qquad \sigma_{av}^{dust} = 1.42 \times 10^{-21}\ \text{cm}^2\ , \qquad n_H = n_{H^0} + n_{H^+}\ , \tag{57}$$

and σ_{ac}^{dust} is the average ionizing photon cross section for absorption and isotropic scattering by dust, per H nucleus, assuming the MRN dust model. Using equation (53) the above constraint on the gas/dust opacity implies that $U \gtrsim 0.06$. We define a critical density,

$$n_c(r) = 3.24 \times 10^8 r_{pc}^{-2} L_{46}\ \text{cm}^{-3}\ , \tag{58}$$

below which $U > 0.06$ and the gas phase emission from the ionized cloud face is diminished to the required level. This value for $n_c(r)$ applies for distances larger than about $4L_{46}^{1/2}$ pc; at smaller distances the grain size distribution is affected due to sublimation of the small grains, the dust opacity declines, and the critical density will be reduced. The lower limit on U obtained above does not take into account various effects such as the change in ionization state with depth inside the slab, and resonance line destruction by dust. An accurate determination of the slab gas phase emission, and the limiting value of U, requires a full photoionization calculation which is beyond the scope of this work.

The gas at a large optical depth is heated by the incident X-rays at a few keV. The energy input will emerge primarily as dust continuum plus IR and FIR atomic and molecular emission (e.g., Krolik & Lepp 1989).

5.3. *The Location of the Dust*

The limiting dust temperature of about 1750 K, translates to a minimum distance of

$$r_{min} \simeq 0.20 L_{46}^{1/2}\ \text{pc} \tag{59}$$

at which even large graphite grains rapidly sublime (Fig. 8). Below we compare this distance with the distances of the broad-line region (BLR) and the narrow-line region (NLR).

The temperature of a blackbody at a given distance, $T_{eff}(r)$, can be parameterized in terms of the associated gas density and ionization parameter, which (given the continuum shape in Fig. 7) gives

$$T_{eff} = 2092 U_{0.1}^{1/4} n_{e,10}^{1/4}\ \text{K}\ , \tag{60}$$

where $U_{0.1} = U/0.1$ and $n_{e,10} = n_e/10^{10}$ cm^{-3}. This value closely corresponds to the temperature of the largest grains, as shown in Figure 8. Note that if the grains reside near the surface of an optically thick cloud then there will also be some diffuse IR flux incident on a grain from below which will raise their temperature by about 10% (see Fig. 13*a*). The effects of dust mixed in with the gas in the BLR clouds were discussed by a number of authors (Baldwin & Netzer 1978; Ferland & Netzer 1979; Martin & Ferland 1980; Rudy & Puetter 1982), who concluded that dust can survive but will be rather hot. Direct measurements of the size of the BLR using line reverberation techniques applied to a number of Seyfert 1 galaxies in recent years (e.g., Maoz et al. 1990; Clavel et al. 1991; Peterson et al. 1991), indicate that the previously accepted values for U, of about 0.01–0.1 (e.g., Kwan & Krolik 1981) and $n_e \sim 10^{9.5}$ cm^{-3}, should both or either be scaled up by about an order of magnitude (e.g., Rees, Netzer, & Ferland 1989; Krolik et al. 1991; Ferland et al. 1992). The new range of values for U and n_e does not allow dust to exist in most of the BLR, at least for low-luminosity AGNs. The largest (and hence coolest) grains might just be able to survive in the outer parts of the BLR in clouds

© American Astronomical Society • Provided by the NASA Astrophysics Data System

1993ApJ...402..441L

with $U \leq 0.03$ or $n_{e,10} \leq 0.3$, if such clouds can be associated with the BLR. Netzer (1990) has suggested that the size of the BLR scales as

$$r_{\rm BLR} \simeq 0.1 L_{46}^{1/2} \text{ pc} \tag{61}$$

in low-luminosity AGNs, which implies that dust can survive just outside the BLR. We note that the broad lines can be reddened only by dust which is significantly outside the BLR, since reddening requires small grains and these survive only at $r \gtrsim 1 L_{46}^{1/2}$ pc.

Photoionization models for clouds in the narrow line region indicate values of $10^{-4} \leq U \leq 10^{-1.5}$, $10^2 \leq n_e \leq 10^6$ cm^{-3} (Osterbrock & Mathews 1986; Osterbrock 1989); at these values small grains will be able to survive. Although not included in most published photoionization models for the NLR, dust mixed in with the gas can have significant effects on the line emission from the NLR, and one might be able to identify the photoionized surfaces of high column density clouds as the sources for the observed narrow lines. These points are currently under investigation.

6. DYNAMICAL CONSTRAINTS

Dynamical effects on dust in AGNs have been considered by Chang, Schiano, & Wolfe (1987) and by Phinney (1989). Here we discuss how radiation pressure effects may constrain our dust models, and also briefly discuss constraints due to tidal effects. Related discussions are given by Mathews & Veilleux (1989) who discuss various instabilities of clouds in the NLR, and by Krolik & Begelman (1988) who discuss the dynamics of molecular clouds in the inner parts of AGNs.

6.1. "*Optically Thin*" *Dust*

Small grains have a high surface area to mass ratio and are therefore subject to a large acceleration when exposed to the continuum source flux. The ratio of the outward radiative acceleration, $g_{\rm rad}$, to the inward gravitational acceleration, $g_{\rm grav}$, on a spherical grain with radius a, and density ρ is given by

$$\Gamma \equiv \left(\frac{g_{\rm rad}}{g_{\rm grav}}\right)_{\rm dust} = \frac{3}{16\pi c a \rho^i G M_{\rm BH}} \int_0^\infty L_\nu Q_{\rm pr}(a, \nu) d\nu \simeq 6.25 \times 10^4 a_{0.1}^{-1} \left(\frac{L_{\rm bol}}{L_{\rm Edd}}\right), \tag{62}$$

where

$$Q_{\rm pr}^i(a, \nu) = Q_{\rm ab}^i(a, \nu) + (1 - g) Q_{\rm sca}^i(a, \nu) \tag{63}$$

is the radiation pressure efficiency of the grain, $M_{\rm BH}$ is the mass of the black hole at the center, $L_{\rm Edd} = 3.24 \times 10^4 L_\odot (M_{\rm BH}/M_\odot)$ is the usual Eddington luminosity, and $a_{0.1} = a/0.1$ μm. The approximation on the right-hand side of equation (62) was obtained assuming $Q_{\rm pr}(a, \nu) = 1$ at all ν, and $\rho^i = 3$ g cm^{-3}. Actual values for the flux weighted mean radiation pressure efficiency, $\langle Q_{\rm pr}(a) \rangle_*$, are shown in Figure 19 for two different shapes of the incident continuum. A continuum source at the Eddington luminosity can therefore accelerate outward grains with $a = 0.05$ μm at about 10^5(!) times $g_{\rm grav}$. The velocity actually attained by the grains depends on the ambient gas pressure, grain charge, and the strength and geometry of the local magnetic field (Draine & Salpeter 1979a, b). Given the gas phase parameters for the "optically thin" case obtained in § 4.1, the grains are likely to become supersonic since the radiation pressure is much larger than the gas pressure. Once the grains attain a velocity of above ~ 100 km s^{-1} (assuming their potential is below ~ 100 V) sputtering will become effective and the grains will be eroded at a rate proportional to the gas density.

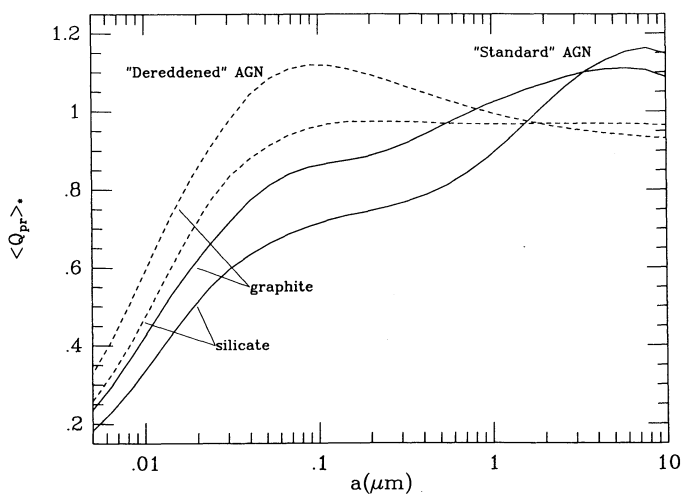

FIG. 19.—Flux weighted mean radiation pressure efficiency for two different shapes of the incident continuum. Solid line corresponds to the continuum shown in Fig. 7 and dashed line corresponds to the incident continuum shown in Fig. 10. In both cases the continuum is assumed to originate from a point source. In the later case $\langle Q_{\rm pr}(a) \rangle_*$ is larger because a larger fraction of the incident flux is in the UV. Note that $\langle Q_{\rm pr}(a) \rangle_*$ remains relatively large even for very small particles since the incident continuum has a significant far UV flux.

© American Astronomical Society • Provided by the NASA Astrophysics Data System

1993ApJ...402..441L

If the grains are strongly coupled to the gas, then we need to consider the opacity of the gas + grain distribution. The ratio of radiative to gravitational acceleration for gas + dust is

$$\Lambda \equiv \left(\frac{g_{\rm rad}}{g_{\rm grav}}\right)_{\rm gas} = \frac{\langle\sigma_{\rm pr}\rangle_*}{\sigma_{\rm es}}\frac{L_{\rm bol}}{L_{\rm Edd}}, \tag{64}$$

where $\langle\sigma_{\rm pr}\rangle_*$ is the dust radiation pressure opacity averaged over the AGN spectrum, and $\sigma_{\rm es} = 6.65 \times 10^{-25}$ cm^2, is the electron scattering cross section per electron. For MRN dust $\langle\sigma_{\rm pr}\rangle_* = 6.29 \times 10^{-22}$ cm^2 per H nucleus, and $\Lambda = 946(L_{\rm bol}/L_{\rm Edd})$. The dust will therefore be expelled together with the gas unless $L_{\rm bol} \ll L_{\rm Edd}$.

The terminal velocity of a gas cloud starting from rest at r_i will be

$$V_{\rm max}(r_i) = \sqrt{2(\Lambda - 1)}V_{\rm Kepp}(r_i) \qquad \text{for } \lambda \geq 1, \tag{65}$$

where

$$V_{\rm Kepp}^2 = GM_{\rm BH}/r^2. \tag{66}$$

The dusty gas will be expelled to a large distance on a time scale of a few $r_i/V_{\rm max}(r_i)$, corresponding to a few times 10^3 yr for gas at a distance of 10 pc, a few times 10^5 yr at a 100 pc, and about 10^7 yr at the outermost radius considered above of 3 kpc. The last time scale is similar to the result of a detailed numerical analysis by Chang et al. (1987) which indicates that all dust grains inside 7 kpc are expelled or destroyed in 3×10^7 yr.

Note that radiation pressure by itself does not preclude the existence of a steady state configuration of "optically thin" MRN dust if a source of dusty gas which supplies about 1 $M_\odot$ yr^{-1} exists close enough to the center. As seen above, however, spectroscopic constraints indicate that a normal MRN composition is ruled out, and such "optically" thin dust must be significantly depleted in silicates. The radiation pressure effects will be significantly reduced if the grain size distribution is dominated by large grains. In the case of $\beta = -1.5$ and $a_{\rm max} = 10$ μm discussed above, $\langle\sigma_{\rm pr}\rangle_* = 7.16 \times 10^{-24}$ cm^2 per H nucleus, $\Lambda = 10.8(L_{\rm bol}/L_{\rm Edd})$ and the dusty gas will not be expelled if $L_{\rm bol} \lesssim 0.1L_{\rm Edd}$, a value which is consistent with some M/L estimates for AGNs.

6.2. *Optically Thick Dust*

In the case of an optically thick cloud with MRN dust we get $\Gamma = 50\tau_{9.7\,\mu{\rm m}}^{-1} L_{\rm bol}/L_{\rm Edd}$, thus radiation pressure is not likely to have a significant effect on the cloud when $\tau_{9.7\,\mu{\rm m}} \geq 10$. The ratio of the incident radiation pressure, $P_{\rm rad}$, to the gas pressure, $P_{\rm gas}$, at the surface of the clouds is related to the ionization parameter by $P_{\rm rad}/P_{\rm gas} = 72U$, for $T_{\rm gas} = 10^4$ K. The lower limit on U of $\sim$0.06 obtained above implies that $P_{\rm rad} > P_{\rm gas}$ at the face of the cloud, so that the grains can develop a significant drift velocity. For a unidirectional radiation field a neutral grain in a 10^4 K gas can be accelerated to a drift velocity of

$$v_{\rm drift} \approx 11 \text{ km s}^{-1} \frac{\psi}{\{1 + [(9\pi/64)\psi]^{1/2}\}}, \tag{67}$$

where $\psi = 8.4\langle Q_{\rm pr}(a)\rangle_* P_{\rm rad}/P_{\rm gas}$ (cf. Draine & Salpeter 1979b, eq. [19]). Charged grains, however, are subject to additional Coulomb drag which may appreciably reduce their drift velocity.

The outer envelope of the cloud will be sheared off by the component of the radiation pressure parallel to the surface, and apart from this effect the photoionized gas at the surface of the cloud will escape in a wind in the absence of a large enough confining pressure. The clouds can also be disrupted by the tidal force of the central black hole, which dominates over the cloud's self-gravity when

$$\frac{GM_c}{r_c^2} < \frac{GM_{\rm BH}r_c}{r^3}, \tag{68}$$

where M_c is the mass of the cloud and r_c is its radius. For a spherical cloud of a uniform density this translates to a critical density, $n_{\rm td} = 10^{10} r_{\rm pc}^{-3} m_9$ cm^{-3}, where $m_9 = M_{\rm BH}/10^9\ M_\odot$, below which the cloud will be disrupted by the tidal force on a dynamical time scale. The cloud density is also constrained to be below $n_{\rm cr} = 3.24 \times 10^8 r_{\rm pc}^{-2} L_{46}$ cm^{-3} by the requirement that $U > 0.06$ at the cloud surface (§ 5.2), and the two constraints can be satisfied only if $r > 2.47(L_{\rm bol}/L_{\rm Edd})^{-1}$ pc, where we have used the relation $L_{46} = 12.5m_9(L_{\rm bol}/L_{\rm Edd})$. In the specific case of circular motion of clouds with $n < n_{\rm td}$ Keplerian shear will stretch the cloud across $2\pi r$, within r/r_c rotations. The clouds might then occupy a torus-like configuration as suggested by Krolik & Begelman (1988). Alternatively, the assumption of a constant cloud density might be incorrect, and the clouds might have a dense core and be self-gravitating, e.g., red giant envelopes (Shull 1983; Scoville & Norman 1988).

We note that both optically thick and optically thin dusty gas cannot remain at a fixed orbit: it will either be expelled, if $\Lambda > 1$, on the time scale discussed above, or, if $\Lambda < 1$, spiral in due to angular momentum loss by the Poynting-Robertson effect. The infall time of the dusty gas from r_i to r_f is given by (e.g., Rybicki & Lightman 1979)

$$t_{\rm PR} = (r_i^2 - r_f^2)\frac{\pi m_p c^2}{L_{\rm bol}\langle\sigma_{\rm pr}\rangle_*} = 1.6 \times 10^4 r_{i,\rm pc}\left(1 - \frac{r_f^2}{r_i^2}\right)(\Lambda m_9)^{-1} \text{ yr} \qquad \text{for } \Lambda < 1, \tag{69}$$

where we assume optically-thin dust and strong coupling of the gas and dust. Γ should replace Λ in the above expression when $t_{\rm PR}$ is smaller than the grain-gas coupling time scale. In the case of an optically thick cloud $\langle\sigma_{\rm pr}\rangle_*$ is to be replaced by the cloud's geometrical cross section per H nucleus in the cloud. This time scale is therefore too long to be important for Keplerian motion at

© American Astronomical Society • Provided by the NASA Astrophysics Data System

1993ApJ...402..441L

$r \gtrsim 100$ pc. It is however interesting to note that the loss of angular momentum results in $V_r(r) \propto r^{-1}$, and mass continuity then implies $n(r) \propto r^{-1}$, i.e., $\gamma = -1$ which is very similar to the value deduced in § 4.1.

7. SIZE AND COMPOSITION MODIFYING PROCESS

There is as yet no convincing explanation for the apparent grain size distribution in the ISM in the Galaxy, and it is therefore premature to try and deduce the size distribution in AGNs from first principles. However, given a size distribution as in our Galaxy one expects the AGN environment to modify this distribution by a number of processes which we briefly discuss below.

1. Temperature fluctuations of very small grains are likely to be large due to the significant flux of far UV and X-ray photons present. The fluctuations induced by absorption of a single X-ray photon will probably eliminate grains with $a \leq 10$ Å as mentioned above, and may deplete grains with $a \leq 50$ Å to a large distance from the center. At $r < 4L_{46}^{1/2}$ pc the steady-state temperature will be high enough to sublime grains with $a \geq 50$ Å (Fig. 8), thus producing a grain size distribution biased toward large grains. Variability of the central source can increase the range of distances over which this process is effective. This process could reduce the dust to gas mass ratio, if the metals which return to the gas phase from the small grains are not able to accrete onto larger grains on a short enough time scale. Grains much larger than 0.25 μm might be able to form by accretion at small distances where all smaller grains sublime.

The time scale for metals to return from the gas to grow large grains is

$$\tau_{\rm acc} = (n_{\rm H}\,\sigma_{\rm geom}\,\Delta v)^{-1}\,, \tag{70}$$

where $\sigma_{\rm geom}$ is the grain geometric area per H nucleus, $\Delta v \equiv \Delta v_5$ km s^{-1} is the mean speed of metal ions relative to the grains, and the grains are assumed to be neutral. For grain model C we find

$$\tau_{\rm acc} = 2.7 \times 10^4 n_6^{-1} \Delta v_5^{-1}\ {\rm yr}\,, \tag{71}$$

where we assume that $\Delta v_5 \lesssim 50$ as otherwise the grain growth is negative due to sputtering. Significant grain growth by this process is therefore much more likely to occur in the case of an optically thick dust configuration due to the relatively high density and low temperature of the gas phase in this case.

2. Grains embedded in a plasma with $T \geq 10^6$ K are subject to thermal sputtering at a rate $\dot{a}(n) \simeq 10^{-2} n_{\rm H}$ Å yr^{-1} (Draine & Salpeter 1979a), which implies a grain lifetime which is proportional to the a. This process can produce a flatter size distribution as shown below. Given a constant injection of grains with a size distribution, $dn/da = Aa^{\beta}$ (for $a_{\rm min} < a < a_{\rm max}$), at a rate $Aa^{\beta}\tau_{\rm inj}^{-1}$, subject to sputtering at a constant rate, then the continuity equation for the resulting size distribution, dn'/da, is

$$\frac{\partial}{\partial a}\left(\dot{a}\,\frac{\partial n'}{\partial a}\right) + \frac{\partial}{\partial t}\,\frac{\partial n'}{\partial a} = \tau_{\rm inj}^{-1} A a^{\beta} \qquad (a_{\rm min} < a < a_{\rm max})\,, \tag{72}$$

which gives for steady-state $dn'/da = Aa^{\beta+1}/\dot{a}\tau_{\rm inj}(\beta + 1)$, i.e., a flatter size distribution. The grain to gas mass ratio will however be lowered by this process.

3. The grains are subject to a high flux of hard photons, and are likely to have a high positive charge due to photoemission of electrons. Once the electric field at the surface of the grain reaches a value of about 3×10^8 V cm^{-1} the grain will be rapidly destroyed (Draine & Salpeter 1979a; Dwek 1987). The effect on the grain size distribution depends in the distribution of $V(a)$, which calls for a detailed calculation of the grain charging processes. The results of Chang et al. (1987) seem to indicate that small grains will be destroyed more efficiently in this process.

We note that the grain potential can also affect the thermal sputtering rate when the potential energy at the surface of the grain is of the order of kT. For example, grains larger than 0.01 μm can support a potential above 300 V; if such a high potential can be achieved it will strongly suppress thermal sputtering in gas at a temperature of $< 3 \times 10^6$ K.

4. Shock processing of grains is likely to deplete silicate grains more than graphite grains (Seab & Shull 1983), thus repeated shock processing in the right velocity range might be able to deplete silicates to a level consistent with observational constraints. Shocks will also preferentially deplete large grains, and enhance the amplitude of the 2175 Å feature (produced by the small graphite grains). This feature should then be quite distinct if the dust is optically thin and lies along the line of sight.

We finally note that the MRN size distribution used in this study is a good description only for dust in the diffuse ISM in our galaxy. Dust in the outer regions of dense clouds in the galaxy is observed to have a modified size distribution (e.g., Mathis 1990), which is consistent with a higher relative abundance of the large grains, probably due to coagulation of small grains rather than growth by accretion from the gas phase. A grain size distribution with a higher fraction of large grains might also be expected if the dust originates in envelopes of cool evolved stars undergoing heavy mass-loss, which were proposed on other grounds to exist near the center of AGNs (e.g., Scoville & Norman 1988; Shull 1983).

8. DISCUSSION

8.1. *Continuum and Broad Line Reddening*

Dust can redden the observed continuum and the broad lines only if it is optically thin in the visible and its size distribution is dominated by small enough grains. Thus optically thick dust or optically thin dust with $a_{\rm max} \gtrsim 1$ μm and a size distribution given by $\beta = -2.5$ or -1.5 cannot have a reddening effect (see Fig. 6). Below we derive limits on the possible reddening effect of optically thin MRN dust, and of MRN-like dust depleted in silicates.

A limit on the fraction of the flux from the continuum source which is reprocessed by the dust can be derived from the observed ratio $L_{\rm IR}/L_{\rm bol} \sim \frac{1}{3}$. This ratio can be produced by silicate-depleted dust (model B, in Table 2), with $\tau_{\rm abs}(1200\ {\rm Å}) = 0.4$ and a dust

© American Astronomical Society • Provided by the NASA Astrophysics Data System

1993ApJ...402..441L

covering factor, C, of unity. This corresponds to a reddening of only $E(B-V) \sim 0.03$. The dust can have an arbitrarily large optical depth if $C \sim \frac{1}{3}$, and can then produce significant reddening if the line of sight intersects the dusty region. Silicate depleted MRN-like dust however produces a significantly more prominent 2175 Å absorption feature per given reddening (Fig. 12). For example we get an absorption depth of 45% in model B versus 15% in the case of MRN dust. Such a large absorption feature can probably be ruled out for most objects (McKee & Petrosian 1974). Preferential depletion of small graphite grains will reduce the 2175 Å feature amplitude, but will also reduce the dust reddening effect, as it is mainly produced by these small grains.

In the case of the MRN dust the absence of a prominent silicate emission feature constrains the dust peak emission to be at $\lambda > 15$ μm, i.e., it should be colder than ~ 200 K. The continuum at $\lambda > 15$ μm has only $\sim 12\%$ of $L_{\rm bol}$, which therefore implies an upper limit on $E(B-V)$ of only 0.012 for the case of $C = 1$, or alternatively $C \sim 0.1$ if the dust has a large optical depth.

We finally note that in some AGNs, in particular Seyfert 2 galaxies, the ratio $L_{\rm IR}/L_{\rm bol}$ is significantly larger than $\frac{1}{3}$, and the upper limits on the amount of reddening are correspondingly higher.

8.2. *Additional Observational Evidence*

Evidence for dust extinction in AGNs based on expected versus observed line ratios from the BLR and the NLR, and on the continuum spectral slope were reviewed by MacAlpine (1985; see also Netzer 1990). Different reddening indicators were found to yield different extinction values, and MacAlpine concluded that "much of the obscuring material is apparently located close to the line-emitting gas". This conclusion is inconsistent with the case of spherically distributed optically thin dust, but might be the result of dust embedded within the narrow line emitting gas, as expected in the case of optically thick dust emission. Carleton et al. (1987) have argued for significant continuum reddening in some hard X-ray-selected Seyfert 1 galaxies, based on their spectral shape and various line and continuum correlations. They also note that in some objects the extrapolated continuum is too steep to explain some observed lines through photoionization, unless a reddening correction is made.

Direct evidence for a column density of a few times 10^{23} cm^{-2} has been found in a number of Seyfert 2 galaxies through absorption of hard X-rays below a few keV (e.g., Awaki et al. 1990). According to recent unification schemes (e.g., Urry, Maraschi, & Phinney 1991) this absorption is due to an obscuring torus of cold gas close to the center, which should also be present in Seyfert 1 galaxies and possibly quasars. Further evidence for large amounts of cold gas, apparently close to the center, comes from the detection of H_2 line emission in a number of Seyfert 1 galaxies and quasars (e.g., Kawara, Nishida, & Gregory 1990). This molecular gas, given a large enough covering factor over a range of distances, could provide an optically thick source for the observed IR emission.

A few of the Seyfert 1 and most of the Seyfert 2 galaxies in the sample of Roche et al. (1991) display the silicate feature in absorption, though its amplitude is usually less than 50%. Starburst galaxies usually display a very strong silicate absorption feature which indicates a high column density of relatively cold silicate dust obscuring a hotter IR emission component. There are some indications for extended starburst activity in Seyfert 2 galaxies (Heckman 1990), and it is possible that the observed spectrum from the center of these galaxies is significantly contaminated by such a component. The luminosity of the nuclear component in Seyfert 1 galaxies, relative to the host galaxy, is usually higher than in Seyfert 2 galaxies, and such contamination effects should be smaller. We note that the dust which produces the low-amplitude silicate absorption feature is unlikely to have a reddening effect in the visible range since a silicate absorption feature requires $\tau_{9.7\ \mu{\rm m}} > 5$ (cf. Fig. 16) and the dust will be optically opaque.

8.3. *Observational Predictions*

Further constraints on the dust configuration, grain composition and grain size distribution in AGNs can be obtained from the following observations:

1. Unless silicate grains with $a \lesssim 3$ μm are highly depleted, a silicate emission feature of some amplitude is likely to be present. High S/N spectroscopy, as will be achieved with future IR missions such as ISO, may reveal either a low amplitude somewhat asymmetric emission feature, as expected if the silicate feature is suppressed by the dominance of very large grains, or a rather symmetric emission feature if it is suppressed mainly due to optical depth effects.

2. A reddened continuum should be accompanied by a significant broad absorption trough centered around ~ 800 Å (Figs. 10 and 12). This feature should have a significantly larger equivalent width than the 2175 Å feature. Its absence would indicate a small amount of carbon or silicate grains significantly smaller than 0.1 μm along the line of sight (cf. Figs. 2, 3), and therefore very little, if any, reddening. Significant constraints on the presence of this feature might be achievable using *HST* observations of $z \sim 1$–2 quasars.

3. Optically thin dust along the line of sight will produce X-ray absorption at low energies. Given the parameters in Table 2, the optical depth at 284 eV (just above the carbon edge) is 12% in model A, and 52% in model D. The associated gas phase opacity will be strongly reduced as it will be highly ionized (§ 5.1). Measuring a small X-ray extinction is, however, complicated by the unknown intrinsic spectral shape of AGNs at low X-ray energy, and the possible presence of additional less ionized gas along the line of sight. Absorption edges provide the clearest signature, and the largest edge is produced by carbon, though the expected flux drop across the edge is quite small. In model A the expected flux drop is 6%, and in model D 2%; the optical depth in model D is much higher than in A but the extinction jump is much smaller (Fig. 6*a*) since the 10 μm grains are opaque at this energy and tend to wash out the edge. The clearest X-ray signature of dust would be the detection of the solid phase shift in the edge energy, of the order of a few eV (e.g., Greaves et al. 1984) due to chemical or solid state effects, as described by Martin & Sciama (1970) and Martin (1970). The detection of these features calls for high S/N X-ray spectroscopy, as may be achieved with AXAF and XMM.

4. The size of the region occupied by very hot dust can be estimated using the near IR (~ 3 μm) flux variability time scale. A more accurate estimate can be obtained using near-IR response time scales to variations in the optical-UV flux (Barvainis 1992). The size of this region can be used to test different dust models. In the case of "optically thin" dust depleted in silicates, but with an MRN-like size distribution, most of the emission comes from the small graphite grains which cannot exist at a distance smaller than

© American Astronomical Society • Provided by the NASA Astrophysics Data System

1993ApJ...402..441L

about $1L_{46}^{1/2}$ pc, whereas if the dust is dominated by large grains most of the emission at 3 μm will come from about $0.2L_{46}^{1/2}$ pc. Optically thick dust can have a significant flux at 3 μm throughout this distance range.

5. The gas phase associated with the dust might also have an observable effect, as mentioned above, either as coronal lines from highly ionized gas associated with "optically thin" dust, or as molecular lines from relatively cold dense gas associated with optically thick dust. The photoionized faces of optically thick clouds will emit narrow lines, possibly similar to the narrow lines observed.

9. SUMMARY

We calculated the optical properties of graphite, silicate and SiC grains over the wavelength range 1000 μm–1 Å for grains in the 0.005–10 μm size range. Both graphite + silicate and graphite + SiC grain mixtures were considered, with various grain size distributions. A detailed radiative transfer calculation was made in order to obtain constraints on the emission properties of dust in AGNs in either "optically thin" or optically thick configurations. The principal results are the following:

1. Warm graphite + silicate or graphite + SiC dust ($T > 200$ K) with the MRN size distribution and a column density $N_H \lesssim 10^{23}$ cm^{-2} produces a strong silicate or SiC emission feature. Such dust cannot be responsible for the observed infrared emission from AGNs.

2. If the observed 10 μm emission comes from dust which is optically thin at 10 μm, then the dust must be either depleted in silicates by at least a factor of 5, or have a grain size distribution extending to $a_{max} = 10$ μm, with a power-law size distribution with $d \ln n/d \ln a \gtrsim -2.5$. Qualitatively similar constraints apply to graphite + SiC dust.

3. MRN dust with a high optical depth at 10 μm produces an emission feature with an amplitude of about 57%, in excess of the typical observational limit for most objects.

4. If the observed 10 μm emission comes from dust which is optically thick at 10 μm, then the dust might either be depleted in silicates by a factor of 2 or more, have a grain size distribution extending to 10 μm with $\beta > -3.5$, be heated at a large optical depth by a source other than the incident optical-UV flux, or some combination of the above. Qualitatively similar constraints apply to a graphite + SiC grain mixture.

5. Reddening of the broad emission lines and continuum is unlikely to be common. MRN dust can have a significant reddening effect only if its covering factor is about 0.1. MRN-like dust depleted in silicates can have a covering factor of about 0.3, and therefore is more likely to intersect our line of sight, but it will also produce a noticeable 2175 Å absorption feature. Dust with a covering factor of about 1 will produce only little reddening [$E(B-V) \leq 0.033$], unless $L_{IR}/L_{bol} \Rightarrow 1$.

6. Dynamical arguments also indicate that high column density dust, and low column density dust dominated by large grains, both of which do not produce a significant ~ 10 μm emission feature or reddening, are more likely to survive the effects of the incident radiation pressure.

7. Dust cannot reside in the BLR clouds if their distance from the continuum source is smaller than $0.2L_{46}^{1/2}$ pc as recently indicated in a few objects. The innermost radius at which even the largest grains can survive is probably just outside the BLR.

8. Dust can reside in the NLR, and might have a significant effect on the gas phase emission when $U \gtrsim 0.01$. If the observed IR emission originates in clouds with $U \gtrsim 0.1$ and $N_H \gtrsim 3 \times 10^{23}$ cm^{-2} then the photoionized cloud face will be a source for narrow-line emission, possibly similar to that observed.

We thank H. Netzer for useful discussions concerning the gas phase emission, and P. G. Martin and J. Krolik for some helpful comments. A. L. acknowledges support by NSF grant PHY91-06210. B. T. D. was supported in part by NSF grant AST90-17082 and NASA grant NAGW-1973.

APPENDIX

THE COUPLING COEFFICIENTS

Below we describe the calculation of the coupling coefficients, $C_\nu^{j,k}$, which relate the average amplitude of the radiation emitted or scattered by one layer to its average incident amplitude in another layer. This derivation applies for the case where both layers have an arbitrary optical depth. A treatment of the coupling of layers having a large optical depth is required here since: (1) the dust opacity varies by more than four orders of magnitude over the wavelength range of interest (Fig. 6); (2) the layer width changes by three orders of magnitude from $\tau_{9.7\ \mu m} \sim 10^{-3}$ at the face of the slab, to $\tau_{9.7\ \mu m} \sim 1$ at the back of the slab.

A.1. $j \neq k$

Given a layer at z_k which extends from $z_k - \Delta z_k/2$, to $z_k + \Delta z_k/2$ and emits a specific power $G_\nu(z_k)$ per unit area parallel to the slab, then the contribution to $F_\nu = cu_\nu$ at z_j, where $z_j \leq z_k - \Delta z_k/2$, is given by

$$F_\nu(z_k, z_j) = \frac{G_\nu(z_k)}{2\Delta\tau_\nu^k} \int_{\tau_\nu^{j,k} - \Delta\tau_\nu^k/2}^{\tau_\nu^{j,k} + \Delta\tau_\nu^k/2} d\tau' \int_0^1 e^{-\tau'/\mu} \frac{d\mu}{\mu} \tag{73}$$

or

$$F_\nu(z_k, z_j) = \frac{G_\nu(z_k)}{2\Delta\tau_\nu^k} \left[E_2\left(\tau_\nu^{j,k} - \frac{\Delta\tau_\nu^k}{2}\right) - E_2\left(\tau_\nu^{j,k} + \frac{\Delta\tau_\nu^k}{2}\right) \right] \tag{74}$$

© American Astronomical Society • Provided by the NASA Astrophysics Data System

1993ApJ...402..441L

where $\tau_\nu^{j,k} = \tau_\nu^k - \tau_\nu^j$, $\tau_\nu^i = \alpha_\nu^{\rm ext} z_i$, and $E_2(x) = \int_0^1 e^{-x/\mu}\, d\mu$ is the second exponential integral. The average value of $F_\nu(z_k, z_j)$ in a layer which extends from $z_j - \Delta z_j/2$, to $z_j + \Delta z_j/2$, defined as

$$F_\nu^{\rm av}(z_k, z_j) \equiv \frac{1}{\Delta\tau_\nu^j} \int_{\tau_\nu j - \Delta\tau_\nu j/2}^{\tau_\nu j + \Delta\tau_\nu j/2} F_\nu(z_k, z_j) d\tau' ,$$

is

$$= \frac{G_\nu(z_k)}{2\Delta\tau_\nu^j \Delta\tau_\nu^k} \int_{\tau_\nu j - \Delta\tau_\nu j/2}^{\tau_\nu j + \Delta\tau_\nu j/2} \left[E_2\left(\tau_\nu^k - \tau' - \frac{\Delta\tau_\nu^k}{2}\right) - E_2\left(\tau_\nu^k - \tau' + \frac{\Delta\tau_\nu^k}{2}\right)\right] d\tau' , \tag{75}$$

or

$$F_\nu^{\rm av}(z_k, z_j) = \frac{G_\nu(z_k)}{2\Delta\tau_\nu^k \Delta\tau_\nu^j} \times \left[E_3\left(\tau_\nu^{j,k} - \frac{\Delta\tau_\nu^k}{2} - \frac{\Delta\tau_\nu^j}{2}\right) + E_3\left(\tau_\nu^{j,k} + \frac{\Delta\tau_\nu^k}{2} + \frac{\Delta\tau_\nu^j}{2}\right) - E_3\left(\tau_\nu^{j,k} + \frac{\Delta\tau_\nu^k}{2} - \frac{\Delta\tau_\nu^j}{2}\right) - E_3\left(\tau_\nu^{j,k} - \frac{\Delta\tau_\nu^k}{2} + \frac{\Delta\tau_\nu^j}{2}\right)\right] \tag{76}$$

where $E_3(x) = \int_0^1 e^{-x/\mu} \mu\, d\mu$ is the third exponential integral.

A.2. $j = k$

The specific power incident on a grain located at z_j inside the emitting layer k, i.e., $z_k + \Delta z_k/2 \geq z_j \geq z_k - \Delta z_k/2$, is

$$F_\nu(z_k, z_j) = \frac{G_\nu(z_k)}{2\Delta\tau_\nu^k} \left[\int_{\tau_\nu j}^{\tau_\nu k + \Delta\tau_\nu k/2} d\tau' \int_0^1 e^{-(\tau_\nu k - \tau')/\mu} \frac{d\mu}{\mu} + \int_{\tau_\nu k - \Delta\tau_\nu k/2}^{\tau_\nu j} d\tau' \int_0^1 e^{-(\tau' - \tau_\nu j)/\mu} \frac{d\mu}{\mu}\right] , \tag{77}$$

or

$$F_\nu(z_k, z_j) = \frac{G_\nu(z_k)}{\Delta\tau_\nu^k} \left[1 - \frac{1}{2} E_2\left(\tau_\nu^j - \tau_\nu^k - \frac{\Delta\tau_\nu^k}{2}\right) - \frac{1}{2} E_2\left(\tau_\nu^k + \frac{\Delta\tau_\nu^k}{2} - \tau_\nu^j\right)\right] , \tag{78}$$

and the average value of $F_\nu(z_k, z_j)$ over the range $z_k + \Delta z_k/2 \geq z_j \geq z_k - \Delta z_k/2$ is

$$F_\nu^{\rm av}(z_k, z_j) = \frac{G_\nu(z_k)}{\Delta\tau_\nu^k} \left\{ 1 - \frac{1}{\Delta\tau_\nu^k} \left[\frac{1}{2} - E_3(\Delta\tau_\nu^k)\right]\right\} . \tag{79}$$

A.3. $C_\nu^{j,k}$

We define the coupling coefficients, $C_\nu^{j,k}$, by the following relation:

$$F_\nu^{\rm av}(z_k, z_j) = C_\nu^{j,k} G_\nu(z_k) , \tag{80}$$

which gives

$$C_\nu^{j,k} \equiv \frac{1}{\Delta\tau_\nu^j \Delta\tau_\nu^k} \left[E_3\left(\tau_\nu^{j,k} - \frac{\Delta\tau_\nu^k}{2} - \frac{\Delta\tau_\nu^j}{2}\right) + E_3\left(\tau_\nu^{j,k} + \frac{\Delta\tau_\nu^k}{2} + \frac{\Delta\tau_\nu^j}{2}\right) - E_3\left(\tau_\nu^{j,k} + \frac{\Delta\tau_\nu^k}{2} - \frac{\Delta\tau_\nu^j}{2}\right) - E_3\left(\tau_\nu^{j,k} - \frac{\Delta\tau_\nu^k}{2} + \frac{\Delta\tau_\nu^j}{2}\right)\right] , \tag{81}$$

for $j \neq k$, and

$$C_\nu^{k,k} \equiv \frac{1}{\Delta\tau_\nu^k} \left\{ 1 - \frac{1}{\Delta\tau_\nu^k} \left[\frac{1}{2} - E_3(\Delta\tau_\nu^k)\right]\right\} . \tag{82}$$

Note that the symmetry relation $C_\nu^{j,k} = C_\nu^{k,j}$ is obeyed.

REFERENCES

Aannestad, P. A. 1992, ApJ, 386, 627
Awaki, H., Koyama, K., Kunieda, H., & Tawara, Y. 1990, Nature, 346, 544
Baldwin, J. A., & Netzer, H. 1978, ApJ, 226, 1
Baribaud, T., Alloin, D., Glass, I., Pelat, D. 1992, A&A, 256, 375
Barvainis, R. 1987, ApJ, 320, 537
———. 1992, ApJ, 400, in press
Bernatowicz, T., Fraundorf, G., Tang, M., Anders, E., Wopenka, B., Zinner, E., & Fraundorf, P. 1987, Nature, 330, 738
Bohren, C. F., & Huffman, D. R. 1983, Absorption and Scattering of Light by Small Particles (NY: Wiley)
Borghesi, A., Bussoletti, E., Colangeli, L., & De Blasi, C. 1985, A&AS, 153, 1
Borghesi, A., Bussoletti, E., Colangeli, L., Orofino, V., Guido, M., & Nunziante-Cesaro, S. 1986, Infrared Phys., 26, 37
Carleton, N. P., Elvis, M., Fabbiano, G., Willner, S. P., Lawrence, A., & Ward, M. 1987, ApJ, 318, 595
Chang, C. A., Schiano, A. V. R., & Wolfe, A. M. 1987, ApJ, 322, 180
Chini, R., Kreysa, E., & Biermann, P. L. 1989, A&AS, 219, 87
Clavel, J., Wamsteker, W., & Glass, I. 1989, ApJ, 337, 236
Clavel, J., et al. 1991, ApJ, 366, 64
Cutri, R. M., Wisniewski, W. Z., Rieke, G. H., & Lebofsky, M. J. 1985, ApJ, 296, 423
Draine, B. T. 1988, ApJ, 333, 848
———. 1989, in IAU Symp. 135, Interstellar Dust, ed. L. J. Allamandola & A. G. G. M. Tielens (Dordrecht: Kluwer), 313
Draine, B. T., & Anderson, N. 1985, ApJ, 292, 494
Draine, B. T., & Lee, H. M. 1984, ApJ, 285, 89 (DL)
Draine, B. T. & Salpeter, E. E. 1979a, ApJ, 231, 77
———. 1979b, ApJ, 231, 438
Duley, W. W. 1973, Ap&SS, 23, 43
Dwek, E. 1987, ApJ, 322, 812
Edelson, R. A., & Malkan, M. A. 1987, ApJ, 323, 516
Efstathiou, A., & Rowan-Robinson, M. 1990, MNRAS, 245, 275
Ferland, G. J., & Netzer, H. 1979, ApJ, 229, 274
Ferland, G. J., Peterson, B. M., Horne, K., Welsh, W. F., & Nahar, S. N. 1992, ApJ, 387, 95
Francis, P. J., Hewett, P. C., Foltz, C. B., Chaffee, F. H., Weymann, R. J., & Morris, S. 1991, ApJ, 373, 465
Glass, I. S. 1992, MNRAS, 256, 23P

© American Astronomical Society • Provided by the NASA Astrophysics Data System

1993ApJ...402..441L

Greaves, G. N., Binstead, N., & Henderson, C. M. B. 1984, in EXAFS and Near Edge Structure III, ed. K. O. Hodgson, B. Hedman, & J. E. Penner-Hahn (NY: Springer), 297
Greenberg, J. M. 1968, in Stars and Stellar Systems, Vol. 7, Nebulae and Interstellar Matter, ed. B. M. M. Middlehurst & L. H. Aller (Chicago: Univ. Chicago Press), 221
Greenberg, J. M., & Hong, S. S. 1974, in IAU Symp. 60, Galactic and Radio Astronomy, ed. F. Kerr & S. C. S. Simonson III (Dordrecht: Reidel), 155
Guhathakurta, P., & Draine, B. T. 1989, ApJ, 345, 230
Hartman, R. C., et al. 1992, ApJ, 385, L1
Heckman, T. M. 1990, in STScI Symposium on Massive Stars in Starbursts, ed. C. Leitherer, N. R. Walborn, T. M. Heckman, & C. A. Norman (Cambridge: Cambridge Univ. Press), 289
Huffman, D. R. 1975, Ap&SS, 34, 175
Hummer, D. G., & Kunasz, P. B. 1980, ApJ, 236, 609
Kawara, K., Nishida, M., & Gregory, B. 1990, ApJ, 352, 433
Korista, K. T., & Ferland, G. J. 1989, ApJ, 343, 678
Krolik, J. H., & Begelmen, M. C. 1988, ApJ, 329, 702
Krolik, J. H., Horne, K., Kallman, T. R., Malkan, M. A., Edelson, R. A., & Kriss, G. A. 1991, ApJ, 371, 541
Krolik, J. H., & Kallman, T. R. 1984, ApJ, 286, 366
Krolik, J. H., & Lepp, S. 1989, ApJ, 347, 179
Kwan, J., & Krolik, J. 1981, ApJ, 250, 478
Landau, L. D., Lifshitz, E. M., & Pitaevskii, L. P. 1984, Electrodynamics of Continuous Media (Oxford: Pergamon)
MacAlpine, G. M. 1985, in Astrophysics of Active Galaxies and Quasi-Stellar Objects, ed. J. S. Miller (Mill Valley: Univ. Science Books), 259
Maoz, D., Netzer, H., Leibovitz, E., Brosch, N., Laor, A., Mendelson, H., Beck, S., Mazeh, T., & Almoznino, E. 1990, ApJ, 351, 75
Martin, P. G. 1970, MNRAS, 149, 221
Martin, P. G., & Ferland, G. J. 1980, ApJ, 235, L125
Martin, P. G., & Rouleau, F. 1991, in Extreme Ultraviolet Astronomy, ed. R. F. Malina & S. Bowyer (NY: Pergamon), 341
Martin, P. G., & Sciama, D. W. 1970, Astrophys. Lett. 5, 193
Mathews, W. G., & Ferland, G. J. 1987, ApJ, 323, 456
Mathews, W. G. & Veilleux, S. 1989, ApJ, 336, 93
Mathis, J. S. 1988, in Dust in the Universe, ed. M. E. Bailey & D. A. Williams (Cambridge: Cambridge Univ. Press), 521
———. 1990, ARA&A, 28, 37
Mathis, J. S., Rumpl, W., & Nordsieck, K. H. 1977, ApJ, 215, 425 (MRN)
McAlary, C. W., & Rieke, G. H. 1988, ApJ, 333, 1
McKee, C. F., & Petrosian, V. 1974, ApJ, 189, 17
Morrison, R., & McCammon, D. 1983, ApJ, 270, 119
Netzer, H. 1990, in Active Galactic Nuclei, SAAS-FEE Advanced Course 20, Swiss Society for Astrophysics and Astronomy, ed. T. J. L. Courvoisier & M. Mayor (Berlin: Springer), 57
Neufeld, D. A. 1990, ApJ, 350, 216
———. 1991, ApJ, 370, L85
Neugebauer, G., Oke, J. B., Becklin, E. E., & Matthews, K. 1979, ApJ, 230, 79
Neugebauer, G., Soifer, B. T., Mathews, K., & Elias, J. H. 1989, AJ, 97, 957
Osterbrock, D. E. 1989, Astrophysics of Gaseous Nebulae and Active Galactic Nuclei (Mill Valley: Univ. Science Books)
Osterbrock, D. E., & Mathews, G. M. 1986, ARA&A, 24, 171
Pegourie, B. 1988, A&AS, 194, 335
Peterson, B. M., et al. 1991, ApJ, 368, 119
Philipp, H. R., & Taft, E. A. 1969, in Silicon Carbide, ed. J. R. O'Connor & J. Smiltens (NY: Pergamon), 366
Phinney, E. S. 1989, in Theory of Accretion Disks, ed. F. Meyer et al. (Dordrecht: Kluwer), 457
Pier, E. A., & Krolik, J. H. 1992, ApJ, 401, in press
Puget, J. L., & Leger, A. 1989, ARA&A, 27, 161
Purcell, E. M. 1976, ApJ, 206, 685
Rees, M. J., Silk, J. I., Werner, M. W., & Wickramasinghe, W. C. 1969, Nature, 223, 788
Rees, M. J., Netzer, H., & Ferland, G. J. 1989, ApJ, 347, 640
Rieke, G. H., & Lebofsky, M. 1981, ApJ, 250, 87
Roche, P. F., Aitken, D. K., Smith, C. H., & Ward, M. J. 1991, MNRAS, 248, 606
Rudy, R. J. 1984, 284, 33
Rudy, J. R., & Puetter, R. C. 1982, ApJ, 263, 43
Rybicki, G. B., & Lightman, A. P. 1979, Radiative Processes in Astrophysics (NY: Wiley)
Ryde, J. W., & Cooper, B. S. 1931, Proc. Roy. Soc. A131, 464
Sanders, D. B., Phinney, E. S., Neugebauer, G., Soifer, B. T., & Mathews, K. 1989, ApJ, 347, 29
Scoville, N., & Norman, C. 1988, ApJ, 332, 163
Seab, C. G., & Shull, J. M. 1983, ApJ, 275, 652
Shull, J. M. 1983, ApJ, 264, 446
Sitko, M. L., & Zhu, Y. 1991, ApJ, 369, 106
Stratton, J. A. 1941, Electromagnetic Theory (NY: McGraw-Hill)
Treffers, R. R., & Cohen, M. 1974, ApJ, 188, 545
Tosatti, E., & Bassani, F. 1970, Nuov. Cimento, 65B, 161
Urry, M., Maraschi, L., & Phinney, E. S. 1991, Comm. Astrophys., 15, 111
van de Hulst, H. C. 1957, Light Scattering by Small Particles (NY: Dover)
Voit, G. M. 1991a, ApJ, 377, 158
———. 1991b, ApJ, 379, 122
Whittet, D. C. B., Duley, W. W., & Martin, P. G. 1990, MNRAS, 244, 427
Woods, D. T., & Draine, B. T. 1993, in preparation

© American Astronomical Society • Provided by the NASA Astrophysics Data System